이학박사 학위논문

Laser-based spectroscopic studies on iron chalcogenide superconductors

철-칼코겐 초전도체에서 레이저 기반 분광학 연구

2023년 2월

서울대학교 대학원

물리천문학부

김 윤 식

Laser-based spectroscopic studies on iron chalcogenide superconductors

지도교수 김 창 영

이 논문을 이학박사 학위논문으로 제출함
2023 년 1 월

서울대학교 대학원
물리천문학부
김 윤 식

김윤식의 이학박사 학위논문을 인준함
2023 년 1 월

위 원 장 _____ 최 현 용
부위원장 _____ 김 창 영
위 원 _____ 장 준 호
위 원 _____ 이 승 섭
위 원 _____ 김 용 관

Laser-based spectroscopic studies on iron chalcogenide superconductors

Younsik Kim

Supervised by

Professor Changyoung Kim

A Dissertation submitted to the Faculty of Seoul National University in Partial Fulfillment of the Requirements for the Degree of Doctor of Philosophy

February 2023

Department of Physics and Astronomy

Graduate School

Seoul National University

ABSTRACT

Laser-based spectroscopic studies on iron chalcogenide superconductors

Younsik Kim

Department of Physics and Astronomy

The Graduate School

Seoul National University

With the discovery of iron-based superconductors, research on strongly correlated systems faced a new era since iron-based superconductors show rich emergent phenomena as well as unconventional superconductivity. Owing to their multiorbital nature, much more degrees of freedom can be imposed, leading to diverse emergent phenomena including various magnetism, nematic phase, and orbital-selective physics. Despite the high interest in iron-based superconductors, their low-energy electronic structures remain a mystery. This is due to their low energy scale in electronic structures due to their low transition temperature and strong renormalization induced by electronic correlations. To reveal the low-energy electronic structures of iron-based superconductors, laser-based spectroscopic measurements can be utilized owing to the high energy resolution of lasers. In particular, low-energy electronic structures can be directly measured by laser-based angle-resolved photoemission spectroscopy (ARPES).

In this thesis, I will present the development of a high-resolution laser ARPES system and experimental results on iron-based superconductors utilizing the setup. The laser is based on optical fibers, which makes the system compact and stable. The output photon energy is 7 eV (177 nm). The ARPES system utilizes a time-of-flight analyzer. Deep learning-based data processing speeds up the slow data acquisition process. The results on iron-based superconductors consist of two parts: i) Kondo lattice in FeTe; and ii) anisotropic superconducting gap in Fe(Te,Se). The successful measurement of low-energy electronic structures with the developed instrument not only facilitates the study of unconventional superconductivity but also leads to the demonstration of a new platform for ARPES.

Keywords: iron-based superconductor, iron chalcogenides, fiber-based laser, angle-resolved photoemission spectroscopy, deep learning, orbital-selective Mott transition, kondo physics, unconventional superconductivity

Student number: 2017-25965

Contents

List of Figures

Chapter 1

Introduction

This chapter provides a brief overview of iron-based superconductors. The background, general phase diagram, and electronic structure of these materials are described. It is then followed by a discussion of iron chalcogenides. The importance of the bond angle in determining the electronic structure of iron chalcogenides is explained in this chapter. Based on the described background, the research motivation for this thesis is discussed.

1.1 Overview of iron-based superconductors

1.1.1 Background of iron-based superconductors

Iron-based superconductors (IBSCs) were discovered in 2008 with a relatively high superconducting transition temperature (T_c). It was a big surprise for the research community as there had been a preconception that superconductivity could not exist in magnetic materials like Fe compounds. Numerous materials have been synthesized since the first discovery. The materials immediately attracted attention due to their similarity to copper-based superconductors (hereafter cuprates). In addition, it is a multiorbital system, which differs from cuprates, which have only a single orbital. Specifically, the similarity of the phase diagram to that of cuprates raised some hope that IBSCs might provide new insight into the microscopic theory of high T_c materials.

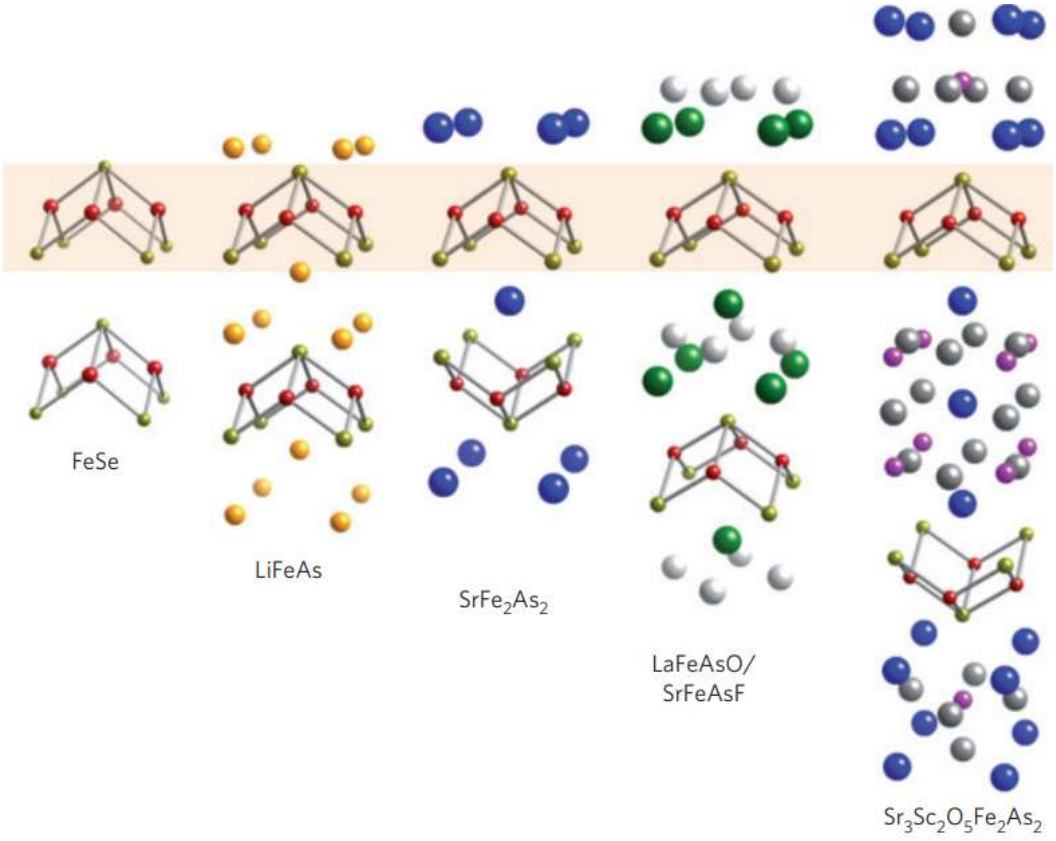

Figure 1.1 Crystallographic structures of the iron-based superconductors.

For the aforementioned reasons, intensive and extensive research has been conducted in IBSCs. Numerous experiments and theoretical studies have been performed on various materials as shown in Fig. 1.2. Even some phenomena emergent in IBSCs have been understood, still numerous physics including the mechanism of the high T_c superconductors have remained unveiled.

1.1.2 Electronic structures

The electronic structure of IBSCs is crucial to understanding their noble physics. As mentioned above, there are numerous system in IBSCs, but overall electronic structure is similar. As shown in Fig. 1.3, the electronic structure mostly consists of t_{2g} orbitals among the Fe 3d orbitals. This multiorbital system makes them distinct from cuprate superconductors, known as a single band system. Detailed explanations of the electronic structure are given as follows. Near the Γ point, three hole bands with d_{xz}, d_{yz}, d_{xy} orbital characters locate. As a consequence, there are several Fermi surface pockets (see Fig. 1.4). Near the Γ point, there are usually two hole pockets while there are two electron pockets near the M point. It is noteworthy that the relative energy level of the hole band near Γ point depends on some parameters, resulting in different Fermi surface topologies.

The detailed electronic structure may vary depending on the system. One of the reasons for this dependence is their crystal structures. The electronic structure of IBSCs are known to be extremely sensitive to the bond angle. The details of the bond angle dependency are discussed in Section 1.2.2.

1.1.3 Multiorbital correlation effects

One of the prominent aspects of IBSCs is their multiorbital nature. Due to the small crystal field splitting and almost half-filled electrons in the Fe 3d shell, the multiorbital correlation effect originated from Hund's coupling dominates the correlation of the systems. Such systems are dubbed as Hund metal. IBSCs are canonical systems that show

Hund metal features such as orbital-selectivity or coherence-incoherence crossover. In this section, the orbital-selective physics of IBSCs is discussed.

The orbital-selectivity is a representative behavior where Hund's coupling dominates the overall correlation [1]. This is due to the strong blocking of interorbital hopping in the presence of Hund's coupling. As a result, the orbital degeneracy is lifted, leading to the tally singlet state (or high spin state). The reduction of possible electron configuration leads to a strong correlation effect. Thus, Hund's metal systems are generally in the strongly correlated regime, where overall spectral functions are broadened and coherent energy scale is significantly suppressed.

IBSCs show various orbital-selective physics [2]. Among them, the orbital-selective Mott phase (OSMP) is the most intensively studied and experimentally confirmed [3]. OSMP is a phase in which only part of the orbitals is in a Mott-localized state. The OSMP is realized in IBSCs, $(Ca,Sr)_2RuO_4$, and some vanadate systems. The OSMP is a result of strong Hund's coupling since Hund's coupling block interorbital hopping. Consequently, the orbitals are separated, behaving individually. Thus, it is possible that one orbital is in a Mott-localized state, whereas other orbitals are in an itinerant state.

1.1.4 Unconventional Superconductivity

IBSCs show unconventional superconductivity. The microscopic pairing mechanism is still unveiled as that of other unconventional superconductors is also unveiled. Still, intensive research until now revealed some features of the origin. The consensus on the

origin of unconventional superconductivity of IBSCs is that pairing is mediated by (π, 0) spin fluctuations, which connect hole- and electron pockets. As a result, the phase of the superconducting gap is shifted by π between each pocket. This is called as s±-wave superconductivity. This s±-wave superconductivity was experimentally confirmed by quasiparticle interference in scanning tunneling microscopy measurements. The inference signal provides information on the phase of each superconducting pocket. Thus, the s±-wave superconductivity was general and representative behavior of IBSCs [4].

Despite the consensus on the s±-wave superconductivity, there are some exceptions. The prime example is a monolayer FeSe grown on $SrTiO_3$ (001) substrate. The measured superconducting transition temperature is up to 100 K, which is enhanced by almost an order of magnitude. The electronic structure measurement by ARPES revealed that the Fermi surface pocket near the Γ point disappears due to the strong charge transfer from the $SrTiO_3$ substrate. This behavior is in strong contrast to the established s±-wave scenario where the Γ point pocket and M point pocket should exist.

Another well-known example is the hole-doped iron pnictide systems. These systems are described as AFe_2As_2 (A = K, Rb, Cs). The hole-doping makes the electron pocket near the M point shrink below the Fermi level [5,6]. This also breaks the conventional s±-wave condition. The resultant behavior of superconducting properties is the emergence of nodal gap structure in such materials. The result regarding the nodal gap structure aroused interest due to possible d-wave superconductivity. However, recent experimental results reported that the superconducting gap symmetry of hole-doped iron pnictides is s-wave, not d-wave.

1.2 Iron chalcogenide superconductors

Iron chalcogenide superconductor is in the IBSC family, having the simplest crystal structures (see Fig. 1.1)[7]. They have a quasi-two dimensional crystal structure. Despite their simple crystal structure, they attracted much attention owing to their rich phenomena. For instance, monolayer FeSe grown on SrTiO3 (001) substrate shows 100 K superconductivities, and $FeTe_{0.5}Se_{0.5}$ shows topological superconductivity. The simple crystal structure but rich phenomena is originated from sensitivity of electronic structures as a function of bond angle. The bond angle can be tuned by chalcogen substitution or by pressure. In this section, brief introductions on the overall phase diagram and bond angle physics are provided.

1.2.1 Overall phase diagram

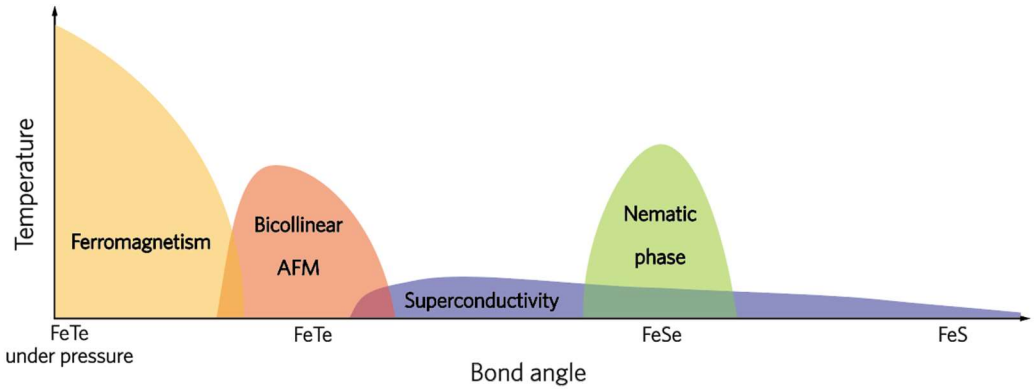

Figure 1.2 Overall phase diagram of iron chalcogenide superconductors.

Overall phase diagram of iron chalcogenide superconductors is illustrated in Fig 1.3. As shown in the phase diagram, iron chalcogenides show rich phenomena, depending on the bond angle. In this regard, the bond angle is a prime parameter describing the physical and electric properties of iron chalcogenides. The superconductivity spans a wide range, covering FeS to $FeTe_{0.9}Se_{0.1}$. However, detailed properties of the superconductivity are different. FeSe shows nematic superconductivity. The superconducting order parameter is strongly anisotropic, following the nematic phase. In $FeTe_{0.5}Se_{0.5}$, topological superconductivity emerges due to the band inversion between the p_z and d_{yz} band. In addition, ferromagnetism and bicollinear antiferromagnetism emerge at pressurized FeTe and FeTe, respectively. In this thesis, the research is focused on FeTe and slightly tuned FeTe (pressurized FeTe and Se-doped FeTe) where strong correlation effect dominates.

1.2.2 Bond angle physics

The rich phenomena shown in iron chalcogenides are due to the sensitivity of electronic structure as a function of bond angle. The chalcogen doping thus significantly changes the electronic structure despite the isovalent doping. In this regard, understanding the role of bond angle is important.

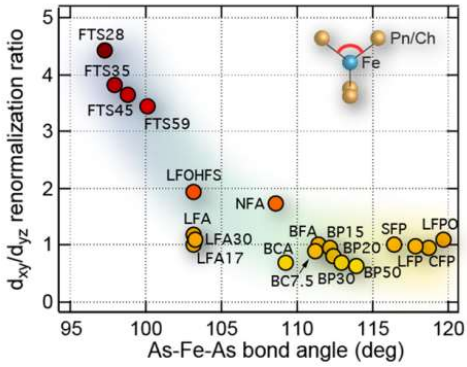

Figure 1.3 Bond angle dependent orbital differentiation in iron chalcogenides [8].

The prime role of bond angle is changing the hopping of each orbital. The hopping of d_{xy} orbital is more suppressed compared to $d_{xz/yz}$ orbitals when the bond angle becomes small. This is due to the fact that the dxy orbital is confined in the Fe plane. If bond angle becomes small, the chalcogen atom is pushed away from the Fe plane assuming bond length is constant. Thus, the hopping of the d_{xy} orbital through the chalcogen atom is suppressed. The phenomenon is represented as OSMP near the FeTe end; the d_{xy} orbital of FeTe is almost completely localized. This orbital differentiated hopping is protected by Hund's coupling, which significantly suppresses interorbital hopping. This orbital-dependent correlation or mass renormalization is well-studied in iron chalcogenide superconductors as shown in Fig 1.3.

1.3 Motivation

FeTe and slightly tuned FeTe show interesting phenomena such as bicollinear

antiferromagnetism, ferromagnetism, and superconductivity. Especially, the transport properties across the magnetic transition change significantly. However, their microscopic origin is still puzzling. This is due to the absence of studies on the low-energy electronic structure of the systems since low-energy electronic structures contain direct information on transport properties and superconductivity. By developing a state-of-the-art high-resolution ARPES system, the low-energy electronic structures of iron chalcogenide can be revealed.

References

[1] Z. P. Yin, K. Haule, and G. Kotliar, Nat Mater **10**, 932 (2011).

[2] P. O. Sprau *et al.*, Science **357**, 75 (2017).

[3] J. Huang *et al.*, arXiv e-prints, arXiv: 2010.13913 (2020).

[4] R. M. Fernandes, A. V. Chubukov, and J. Schmalian, Nature Physics **10**, 97 (2014).

[5] F. Hardy *et al.*, Physical Review B **94** (2016).

[6] D. Zhao *et al.*, Physical Review B **97**, 045118 (2018).

[7] J. Paglione and R. L. Greene, Nature physics **6**, 645 (2010).

[8] M. Yi, Y. Zhang, Z.-X. Shen, and D. Lu, npj Quantum Materials **2** (2017).

Chapter 2

Development of laser-based ARPES system

In this chapter, experimental setups are introduced which are utilized to obtain the results in this thesis. Along with overall scheme and working principles, detailed descriptions on each component are provided. Since the main purpose of the thesis is to study and investigate low-energy electronic structures of iron chalcogenide superconductors, developing a system with high energy-resolution is approach. In this regard, the distinct points that make different from other ARPES system are described. More specifically, next-generation time-of-flight analyzer and fiber-based laser are utilized, which are totally different approach from conventional ARPES setup. The developed setup has a high energy-resolution of 1.4 meV without space-charge effect.

This chapter is organized as follows. Firstly, time-of-flight analyzers are introduced with the comparison with hemispherical analyzers. Next, fiber-based lasers and detailed experimental setups are described. Finally, overall ARPES setup, representative data are introduced.

2.1. Angle-resolved photoemission spectroscopy (ARPES)

2.1.1. Introduction to ARPES

Angle-resolved photoemission spectroscopy (ARPES) measures electron distributions in the reciprocal space of solids directly. As a result of the photoelectric effect, electrons are emitted from the sample when light is incident upon it. The photoelectrons have information regarding their kinetic energy and emitted angle. Based on this information, it is possible to determine the binding energy and momentum of the electrons in the crystal (see Fig. 2.1). The following explanations provide more detail.

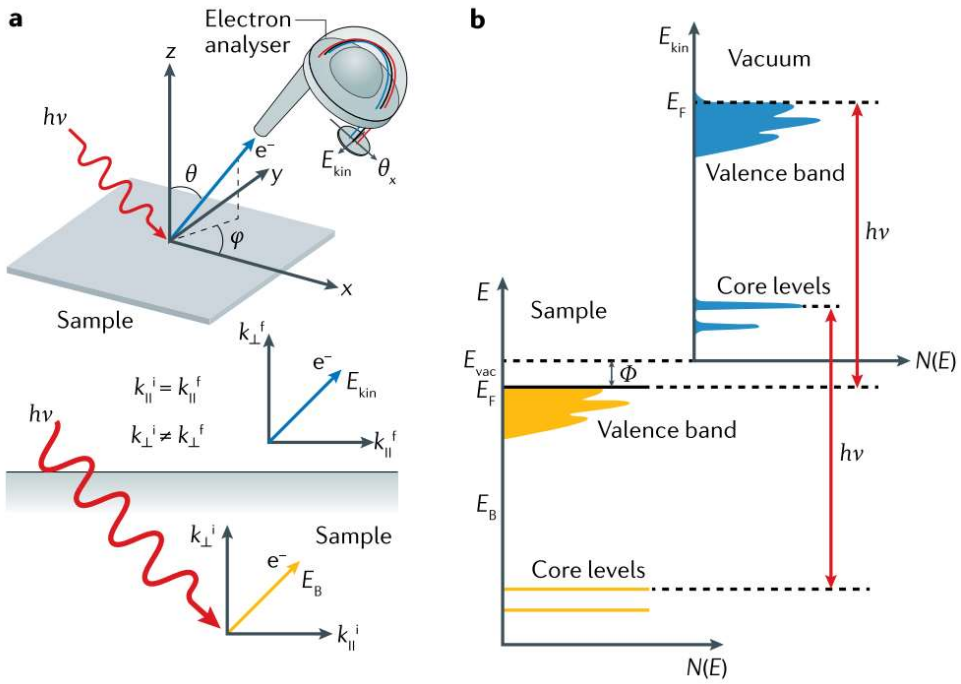

Figure 2.1 Schematic illustrating ARPES process [1].

The photoelectron have information as follows:

$$\hbar k_x = \sqrt{2mE_{kin}} \sin\theta \cos\varphi$$

$$\hbar k_y = \sqrt{2mE_{kin}} \sin\theta \sin\varphi$$

$$\hbar k_z = \sqrt{2mE_{kin}} \cos\theta$$

where E_{kin} is the kinetic energy of the photoelectrons. In principle, the electronic structure can be obtained with the information of E_{kin}, θ, and φ. However, the out-of-plane momentum is not conserved through the photoemission process since translational symmetry is broken at the surface. Therefore, additional information is required to obtain out-of-plain momentum k_z. Assuming that the dispersion of the final state of photoelectrons as a free electron, the final state energy reads as follows:

$$E_f(k) = \frac{\hbar^2 k_{\parallel}^2 + \hbar^2 k_{\perp}^2}{2m} - E_0$$

where E_0 is the bottom energy of the valence band and m is an electron mass. Moreover, together with two equations below,

$$E_f(\mathrm{k}) = E_{kin} + \phi$$

$$\frac{\hbar^2 k_{\parallel}^2}{2m} = E_{kin} \sin\theta^2$$

where ϕ is a work function of a sample during photo-emission process. Then, out of plane momentum $k_{\perp}$ (k_z) can be determined as follows.

$$k_{\perp} = \frac{1}{\hbar}\sqrt{2mE_{kin}\cos\theta^2 + V_0}$$

where V_0 ($= E_{kin} + \phi$) is an inner potential. Changing photon energy of light source, V_0 can be obtained experimentally by using the boundary condition of periodicity in $k_{\perp}$ (equivalent to photon energy). As a result, electronic state of the solids can be determined from the combination of ARPES experiment and the principles explained above. ARPES can provide the information of electronic spectra with energy dispersion and Fermi surface maps.

From above, ARPES can provide the direct information of the electronic structure of solids in energy-momentum space. About the experimental (instrumental) aspect of ARPES, in general, the system consists of various instruments such as an electron analyzer, light sources, a manipulator with temperature control, several vacuum pumps to achieve ultra-high vacuum (pressure better than 5 x 10^{-11} Torr) and other *in situ* experimental instruments to perturb the sample under measurement with electric field, electron doping, strain, and so on. Finally, let us provide the detailed information of the instruments in the following subsections and our installed home lab *in situ* ARPES system.

2.1.2 Electron analyzer

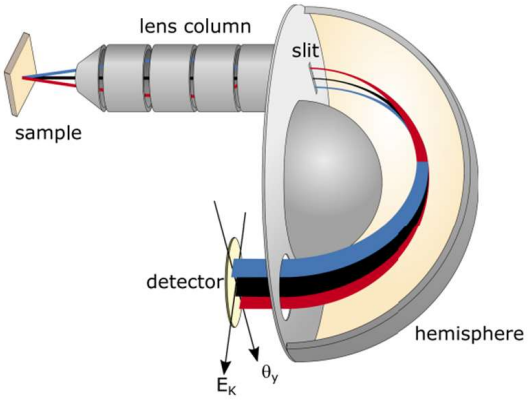

Figure 2.2 Schematic drawing of a hemisphere electron analyzer [2].

To detect and analyze the photo-electrons from a sample, various type of electron analyzers have been developed. Among them, hemisphere analyzer is the most common method to resolve the energy and momentum of electrons by bending the electron path with an electromagnet as shown in Fig. 2.2.

Brief process of detecting photo-electrons inside the analyzer can be explained as follows. As in Fig. 2.2, the analyzer utilizes a hemisphere electromagnet for bending path of electron to resolve the energy. In detail, firstly, the photo-electrons enter to an electron-lens table ahead of entering the electromagnet. Then, electric field from the lens set a certain kinetic energy of electrons to a defined energy called pass energy (E_P). The rest of electrons with kinetic energy other than the set certain kinetic energy, is affected by the lens and enter into slits. As a result, photo-electrons of energy near E_P selectively enter into the hemisphere. Inside the hemisphere, magnetic field is applied for bending path of the electrons (entered into slit) and its magnitude is set to make the electron of E_P reach onto a center of a two-dimensional (2D) measuring device, the detector. For other

electrons, electrons with $E > E_P$ are bent less while those of $E < E_P$ bent more. Finally, the photo-electron energy is resolved as the final electron positions on the 2D detector as shown in Fig. 2.2.

For some detailed information of data acquisition can be provided. Firstly, the angle θ of photo-electron as in Fig. 2.12, can be directly resolved as the final electron positions on the 2D detector by using the momentum conservation law if the photo-electron successfully enter into the slit. From the fact, to obtain information of the angle φ perpendicular to the slit direction, the sample has to be rotated in the direction by using manipulator. To sum, information of θ and φ can be obtained by analyzer and by controlling the angle (relative to the slit geometry) of sample, respectively.

On the other hand, details of detector units can be explained. The hemisphere analyzer usually consists of three steps of detector units: (1) Final electrons hit multi-channel plate of nano-sized arrays of electron multiplier which amplifies the signal enough to be measured. (2) Amplified bunch of electrons hit a scintillator converting light signal from charged particles. (3) The light is measured by 2D CCD which resolves an angle axis (θ) and an energy axis.

2.1.3 Light sources

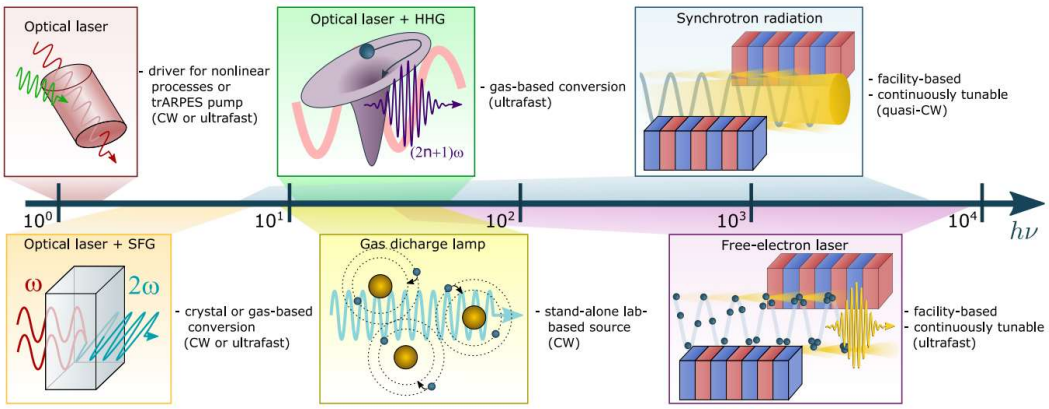

Fig 2.3 Various types of light sources for ARPES with their characters and photon energy ranges [2].

In addition to the analyzer, light source is also a fundamental instrument for ARPES measurement and thereby, various types of light sources have been developed as shown in Fig. 2.3. In general, typical light sources to induce photo-electrons of solids for ARPES measurement are threefold by using a synchrotron radiation, a gas discharge lamp, and an optical laser. A critical requirement to be utilized as a light source would be that the photon energy has to be larger than work function of samples, which typically is around 4.5 eV for many cases. From now on, we will introduce the characteristic light sources (synchrotron radiation & discharge lamp) in this subsection one by one.

The most common example would be the synchrotron radiation which can provide a change in photon energy. It generates light by bending (accelerating) the propagating bunches of electrons which induces light emission. Moreover, synchrotron radiation utilizes a set of magnets (called undulator) to manipulate the emitted photons, which can

provide a manipulation of photon polarizations and energy. On the other hand, high flux compared to those of discharge lamp or laser would provide various advantages for ARPES measurement: (1) Obtained data have less noise level, better statistics, and thereby a short data acquisition time. (2) Large flux allows a much small beam size (typically about few tens of microns in diameter) providing sufficient numbers of photoelectrons. (3) Corresponding small beam size provides fine momentum-, energy-resolutions, and also opens a way for measurement of tiny size samples.

Another frequent example would be a gas discharge lamp which utilizes gases (typically He, Xe, Ne) with low pressure. Among the gases, He gas would be the most common element providing photon energy of 21.2 eV (He I) and 40.8 eV (He II) [3,4]. Since the discharge lamp can be run with a compact controller and the unit size is not that large, it usually is installed in many home lab based ARPES facilities. However, since the gas determines photon energy, the energy cannot be varied compared to the case in synchrotron radiation which makes the lamp not suitable for measurement of materials having three-dimensional electronic structures.

2.2 Time-of-flight analyzers

Advances in spectroscopic techniques often accompany an increase in the dimension that can be obtained, thereby allowing new information. The prime example of this is ARPES. Conventional hemispherical analyzers can take two-dimensional energy/momentum space, whereas modern-day angle-resolved time-of-flight (ARTOF)

analyzer can take three-dimensional energy/momentum space [2]. Despite their capability that can cover additional phase space thereby allowing new information, most of ARPES analyzers are still hemispherical analyzers to date due to some apparent shortcomings of ARTOF analyzers. In this section, the working principle of ARTOF analyzers which is totally different from that of hemispherical analyzers is introduced. The advantages and disadvantages of ARTOF analyzers over hemispherical analyzers are described as well, with newly developed methodologies to alleviate such shortcomings of ARTOF analyzers.

2.2.1 Working principles

ARTOF analyzers measure flying time of photoelectrons from sample surface to the detector to measure the kinetic energy of photoelectrons. Without any lens voltages, the conversion relation between flying time and kinetic energy of photoelectrons are as follows:

$$E_k = \frac{m_e}{2}\left(\frac{L}{t}\right)^2$$

where m_e is mass of electrons, L is distance from sample surface to detector, and t is flying time of photoelectrons. To measure the kinetic energy in meV scale, detectors should have temporal resolution in several hundreds picosecond scale. Since conventionally used charged charge-coupled device (CCD) detectors have much slower temporal resolution, a new type of detector called as delay line detector (DLD) combined with microchannel plate (MCP) is utilized in ARTOF analyzers. DLDs contain several

layers of grid-like electrodes as shown in Fig. 2.4. A bunch of multiplied photoelectrons emitted from MCP bumps into the grid-like electrodes, resulting in two counterpropagating pulses in each electrode. Ends of each electrode are connected to a time-to-digital converter (TDC) board where incoming timings of pulses are digitized. The x, y positions can be calculated by the timing difference between each end of electrodes. The conversion relation is as follows:

$$x = x_0 + v(t_{x1} - t_{x2}), y = y_0 + v(t_{y1} - t_{y2})$$

where v is transverse propagating speed of pulses in electrodes and t_{i1}, t_{i2} are timings at the end of each electrode along *i*-direction. In the same manner, total flying time can also be calculated by averaging the two timings. Measured (x, y, t) data has one-to-one correspondence to (k_x, k_y, E) data. However, complex non-linear conversion should be applied to obtain (k_x, k_y, E) data from (x, y, t) data. Roughly speaking, each axis of measured (x, y, t) signals roughly corresponds to the each axis of (k_x, k_y, E).

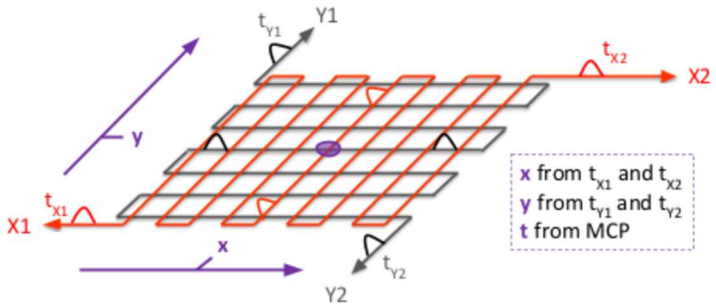

Figure 2.4 Schematic drawing of delay line detectors.

2.2.2 Comparison with hemispherical analyzers

The novel combination of DLD and MCP enables new information of photoelectrons; simultaneous three-dimensional data acquisition gives two-dimensional momentum resolution as well as energy resolution. In contrast, hemispherical analyzers can obtain two-dimensional data. To get data from two-dimensional Brillouin zone, sample should be rotated, or photoelectron should be deflected with proper lens tables. The simultaneous acquisition of three-dimensional energy/momentum space accelerates data acquisition and makes matrix element effect simpler. In addition, hemispherical analyzers utilize slits to have energy resolution [2]. Thus, most of photoelectrons are blocked, resulting in low photon-detector count conversion efficiency. The low photon-detector count conversion efficiency is detrimental for high resolution measurements, where space-charge effect should be severely considered (see Fig. 2.5) [5,6]. This, in turn, implies that the data acquisition efficiency becomes worse when it comes to high resolution measurements. ARTOF analyzers are slitless. The photon-detector count conversion efficiency is much better compared to hemispherical analyzers. As a result, the measurement efficiency for high-resolution measurements is much better compared to hemispherical analyzers.

Despite these advantages of ARTOF analyzers, ARTOF analyzers have not been adopted so much for their apparent disadvantages. The prime disadvantage is a constraint on light source: the light source should be pulsed with proper pulse width and repetition rate. More specifically, the pulse width should be less than 1 ns for meV-scale energy resolution, and repetition rate should be in range from 100 kHz to 1.5 MHz. These

required conditions strongly impose constraints on light source. Continuous wave light sources, which have been conventionally used such as gas discharge lamps, cannot be used with ARTOF analyzers. Only some of lasers or synchrotron light sources can be used for ARTOF analyzers. Another known issue of ARTOF analyzers is slow data acquisition for lower-dimensional data. If one only needs energy/momentum cuts or just energy distribution curve, hemispherical analyzers are much faster for such applications.

These features are apparent obstacles to prevent ARTOF analyzers from being widely used. In this thesis, the disadvantages are overcome by introducing a home-built fiber laser and deep learning-based data processing techniques [7], which will be introduced later.

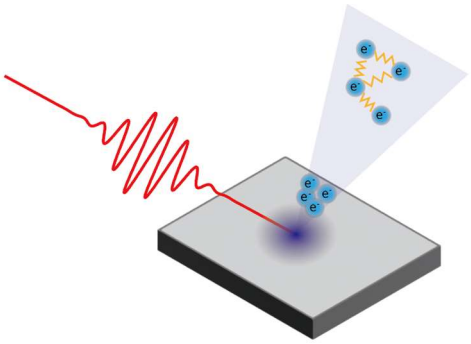

Figure 2.5 Space-charge effect for ARPES measurements.

2.3 Fiber-based 7 eV laser

Since the successful application of lasers as a new light source for ARPES measurements, high-resolution (HR) measurements enabled by lasers allow for new

information, thereby facilitating new discoveries. The most widely used laser for ARPES is 7 eV laser, which is 6-th harmonics of Nd:YVO_4 laser which generates 1064 nm [8,9]. The generation of 7 eV (177 nm) light is enabled by the development of $KBe_2BO_3F_2$ (KBBF) crystals, which can convert 3.5 eV photons into 7 eV photons. The combination of the KBBF crystals and Nd:YVO_4 is widely accepted, opening a new era in laser ARPES.

2.3.1. Motivation: why fiber-based lasers?

Fiber-based lasers attracted much attention recently due to their compact, and stable properties [6,10]. Compared to bulk solid-state lasers, fiber-based lasers occupy much smaller space. In addition, fiber-based lasers do not require any alignment, which guarantees stability over a long time. These features are ideal for spectroscopic experiments. Thus, some research group starts to apply fiber-based lasers in spectroscopic experiments [6,11]. In addition, fiber-based lasers feature high amplifier gain (up to 30 dB) [12]. This, in turn, means that complicated amplification structures such as regenerative amplifiers are not required. For spectroscopic experimentalist, such easy-to-handle features of fiber-based lasers are another attractive point.

The weak point of fiber-based laser is non-linear effects in fiber medium; when intense light pulses propagate the laser medium, undesired phenomena such as self-phase modulation, self-focusing, and non-linear polarization rotation occur [13]. These phenomena are detrimental for fiber lasers, which should be avoided. Considering intense

pulses cause the non-linear effect, the peak power or pulse energy is limited. This severely limits the output power from fiber-based lasers.

ARTOF analyzers require much less power of light sources compared to hemispherical analyzers owing to the slitless nature. Thus, the disadvantage of fiber lasers: weak output power is not a remarkable problem for ARTOF analyzers. This makes ARTOF analyzers and fiber-based lasers a novel combination.

2.3.2. Overall structure

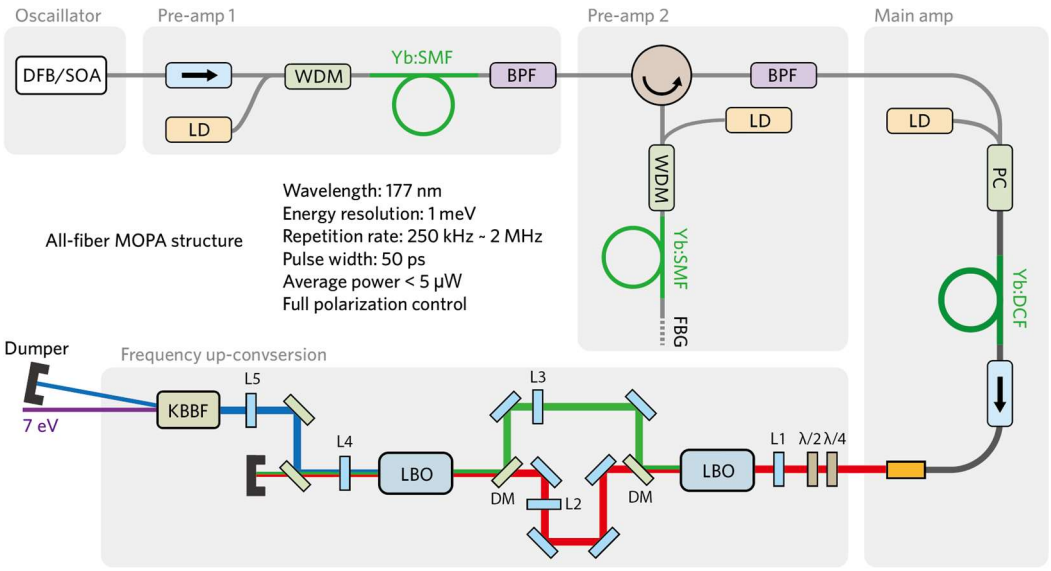

Figure 2.6 Schematic of fiber-based 7 eV laser. DFB: distributed feedback laser; SOA: semiconductor optical amplifier; LD: laser diode; WDM: wavelength division multiplexer; BPF: bandpass filter; PC: pump combiner; SMF: single mode fiber; DCF: double-clad fiber; FBG: fiber Bragg grating; LBO: LiB_3O_5 crystal.

The overall schematic of fiber-based 7 eV laser is illustrated in Fig. 2.6. Gain switched distributed feedback laser (DFB) module is utilized as an oscillator. The weak pulse generated subsequently amplified by a semiconductor optical amplifier (SOA) located in the same module. The series of amplification stages made of Yb-doped fiber is fed by optical pulses generated from DFB/SOA module. The oscillator and amplifiers are all fiber setups, which is dubbed as the master oscillator fiber amplifier (MOFA) setup. The frequency of amplified pulses is up-converted to 6th harmonics by a series of LiB_3O_5 crystals and a KBBF crystal. Fig. 2.7 shows the fiber-based 7 eV laser system built in the home lab.

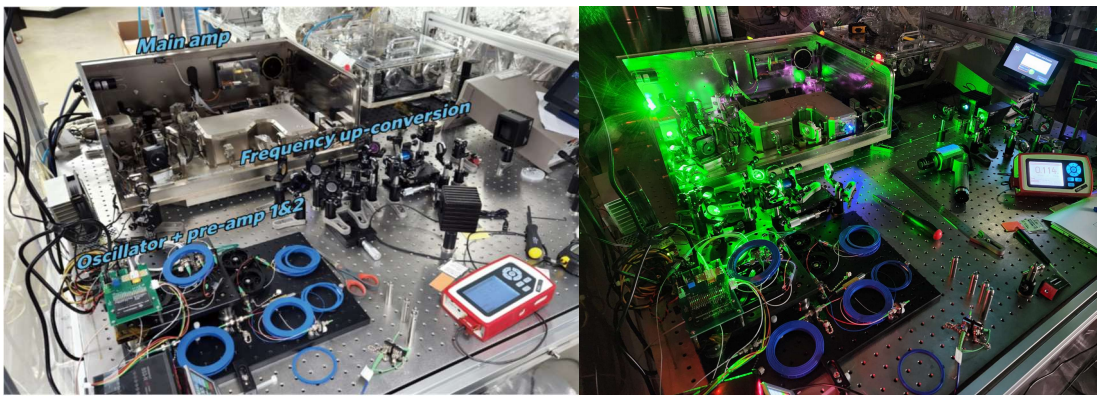

Figure 2.7 Fiber-based 7 eV laser system built in Seoul National University.

2.3.3. Oscillator: gain-switched DFB laser diode

For the oscillator of the laser system, gain-switched DFB laser diode is adopted. The adopted reasons are as follows:

i) Stable pulse generation

Since optical pulses with pulse width of 50 ps can be generated by electrical switching, stable pulse generation free from external perturbation is possible. This feature is in a strong contrast with mode-locked lasers, in which pulse generations are severely affected by external perturbation such as temperature fluctuations or mechanical vibrations. The stability of pulse generation of DFB laser diodes enables the operation of lasers at ambient conditions.

ii) Free repetition rate tuning

Considering the working principles of ARTOF analyzers, free repetition tuning is a desirable feature. If repetition rate is too high, the photoelectrons are overlapped with subsequent photoelectrons. If repetition rate is too low, data acquisition is slow and space-charge effect is more significant. Since the optimal repetition rate depends on lens mode, tunability of the repetition rate is highly desirable.

iii) Easy integration with fiber amplifiers

Since the output of DFB/SOA module is connected by optical fibers, it is easy to integrate with fiber amplifiers. This enables all-fiber setup, which does not require alignment procedure. This ensures long-term stability of the MOFA system.

Considering the advantages of gain-switched DFB laser diodes over mode-locked lasers, the DFB laser diode module (QCBA1061-64A0 from QDLaser) is adopted.

2.3.4. Amplifier: Yb-doped fibers

Yb-doped fibers are utilized for the amplification stages. The output from DFB/SOA module are connected to the Yb-doped fiber amplifiers by FC/APC connectors. The amplification stages consist of three stages: two pre-amplification stages and one main amplification stage. First pre-amplifier utilizes Yb-doped fibers with core diameter of 4 μm, cladding diameter of 125 μm, and core absorption at 976 nm of 1200 dB/m (LIEKKI, YB-1200-4/125). Second pre-amplifier utilizes Yb-doped fibers with core diameter of 6 μm, cladding diameter of 125 μm, and core absorption at 976 nm of 250 dB/m (Coherent, SM-YSF-HI-HP). The pre-amplification stage utilizes single-mode 976 nm laser diodes (Thorlabs, BL976-SAG300) as pump sources. The current and temperature of laser diodes are precisely controlled for stable operations. Fiber-based isolators are installed in between amplification stages to protect from back-propagating light. Fiber-based bandpass filters are also installed after each stage, to block amplified spontaneous emission. Second amplification stage is double-pass scheme, by using a fiber Bragg grating and a fiber circulator. The fiber Bragg grating not only act as a mirror reflecting 1064 nm pulses but also act as a bandpass filter. The average power of pre-amplified pulses is around 50 mW at 1.5 MHz. The average power is amplified up to 1 W after main amplification stage.

2.3.5. Frequency up-conversion

The amplified 1064 nm pulses are up-converted series of LBO and KBBF crystal. First, 1064 nm pulses are up-converted to 532 nm by an LBO crystal. The second harmonic generation is in type I non-critical phase matching (NCPM) condition where the phase matching condition is set by temperature. The intrinsic pulse and second harmonic pulse are fed into second LBO crystal where third harmonic pulses are generated via sum-frequency generation. The sum-frequency generation is in the type II phase matching condition. Subsequently, the 6^{th} harmonics are generated in the KBBF crystal inside a nitrogen chamber. Generation of 6^{th} harmonics is checked by a vacuum ultraviolet (VUV) sensitive photodiode from Hamamatsu.

2.3.6. 7 eV alignment/focusing

Since 6^{th} harmonics or 7 eV light cannot propagate in the air due to strong absorption by oxygen or vapor water, all 7 eV alignment and focusing are performed inside a custom-made acrylic optical chamber. The optical chamber is always filled with nitrogen or argon gas. When aligning optics inside the chamber, the chamber is filled with argon which is much heavier than air. Thus, the alignment can be conducted with the lid of the chamber open. This makes the whole alignment procedure much easier and is in strong contrast with 11 eV, which requires a much purer condition.

Focusing 7 eV light onto the sample surface is done by using a pair of CaF_2 lenses. One is used for collimating divergent 7 eV light from the KBBF crystal, and the other one is

used for focusing the light onto the sample. The focused beam spot size is less than 100 μm, checked by knife-edge method and phosphorus sample.

2.4 Laser-based ARPES system

The ARTOF analyzer and developed fiber-based 7 eV laser are combined, along with an open-cycle cryo-manipulator that can cool down to 5 K and 6-axis motion. In this section, the overall structure, representative data, and system benchmark are represented.

2.4.1 Overall structure

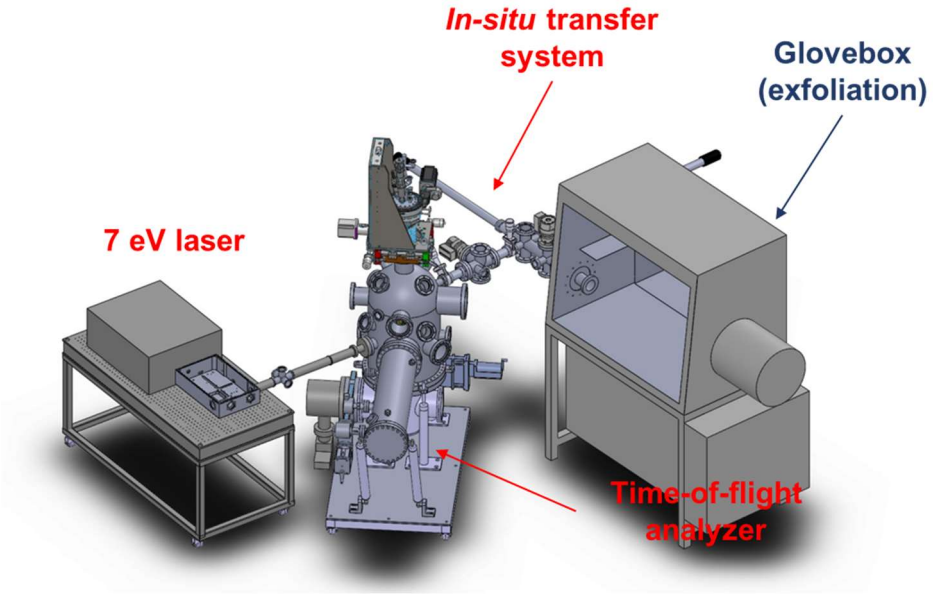

Figure 2.8 Schematic illustration of laser-based ARTOF system.

The overall structure of the laser-based ARPES system is illustrated in Fig. 2.8. As well

as the laser system and ARTOF analyzer, the laser-based ARPES system has a glovebox and *in situ* transfer system. By utilizing the setup, air-sensitive or exfoliated samples can be prepared and transferred without exposure to air. In addition, an ultra-high vacuum suitcase enables us to transfer samples from thin film growth chambers. This versatility extends the sample spectrum from single crystals to artificially fabricated systems such as thin films or exfoliated systems.

2.4.2 Representative data and benchmark

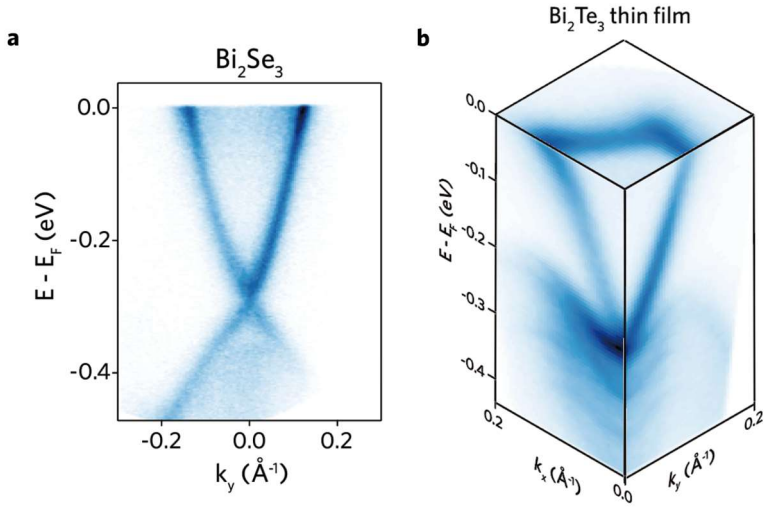

Figure 2.9 Representative data from the developed laser-based ARPES system. a. ARPES data from a Bi_2Se_3 single crystal. b. ARPES data from a Bi_2Te_3 thin film.

Representative data from the developed laser-based ARPES system is illustrated in Fig. 2.9. Shown in Figs. 2.9a and b are from Bi_2Se_3 single crystal and Bi_2Te_3 thin film, respectively. The results show clear spectra with well-defined band structures. ARPES

data from these reference samples show the developed ARPES system works well with good data quality.

To investigate the performance of the ARPES system quantitatively, we conducted energy resolution measurements. Shown in Fig. 2.10 is the temperature-dependent ARPES measurement result on superconducting $FeTe_{0.55}Se_{0.45}$. Note that the superconducting transition temperature of $FeTe_{0.55}Se_{0.45}$ is around 15 K. The low-temperature data shows a well-defined quasiparticle peak (QP), whereas high-temperature data shows the edge following the usual Fermi-Dirac distribution. The edge of the QP seen in low-temperature data has a width of around 1 meV, directly demonstrating the energy resolution of the system. Note that the results are taken without attenuating photon flux, which demonstrates high resolution of 1 meV can be obtained without the space-charge effect.

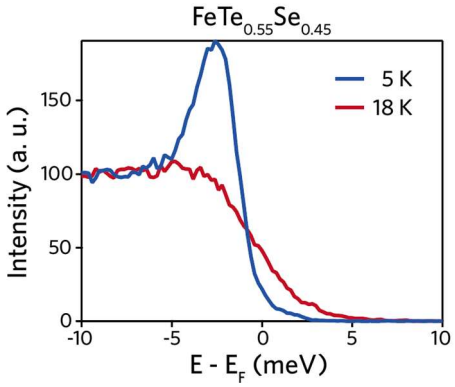

Figure 2.10 Temperature-dependent ARPES results on $FeTe_{0.55}Se_{0.45}$.

Up to now, I have provided explanations for experimental setups for the research in this thesis. Based on the experimental tool, in the following chapters 3 and 4, my main

results and discussion of the low energy physics of iron chalcogenide superconductors are covered.

References

[1] B. Lv, T. Qian, and H. Ding, Nature Reviews Physics **1**, 609 (2019).

[2] J. A. Sobota, Y. He, and Z.-X. Shen, Reviews of Modern Physics **93**, 025006 (2021).

[3] N. Shevchik, Journal of Electron Spectroscopy and Related Phenomena **14**, 411 (1978).

[4] T. Durakiewicz, A. Arko, J. J. Joyce, D. P. Moore, and K. Graham, Review of scientific instruments **73**, 3750 (2002).

[5] S. Hellmann, T. Ott, L. Kipp, and K. Rossnagel, Physical Review B **85**, 075109 (2012).

[6] Y. Ishida, T. Otsu, A. Ozawa, K. Yaji, S. Tani, S. Shin, and Y. Kobayashi, Review of Scientific Instruments **87**, 123902 (2016).

[7] Y. Kim *et al.*, Review of Scientific Instruments **92**, 073901 (2021).

[8] T. Kiss *et al.*, Rev Sci Instrum **79**, 023106 (2008).

[9] G. Liu *et al.*, Review of Scientific Instruments **79**, 023105 (2008).

[10] S. Kim, S. Jung, B. Seok, Y. Kim, H. Park, T. Otsu, Y. Kobayashi, C. Kim, and Y. Ishida, Review of Scientific Instruments **92**, 043905 (2021).

[11] A. Mills *et al.*, Review of Scientific Instruments **90**, 083001 (2019).

[12] J. Limpert, T. Schreiber, T. Clausnitzer, K. Zöllner, H.-J. Fuchs, E.-B. Kley, H. Zellmer, and A. Tünnermann, Optics Express **10**, 628 (2002).

[13] C. Jauregui, J. Limpert, and A. Tünnermann, Nature photonics **7**, 861 (2013).

Chapter 3

Kondo interaction in FeTe

In this chapter, I provide the results to confirm/clarify the existence of Kondo lattice behavior in FeTe. As well as the drastic change of transport properties across the magnetic transition, the peculiar magnetism of FeTe can be explained under the Kondo lattice scenario. The observation was enabled by the high energy resolution of the developed laser-based ARPES system, which can directly measure low-energy electronic structures of FeTe. The strongly enhanced electron mass is a representative feature of Kondo lattice or resultant heavy fermion (HF) behavior which was elusive up to date.

Finding d-electron heavy fermion (HF) states has been an important topic as the diversity in d-electron materials can lead to many exotic Kondo effect-related phenomena or new states of matter such as correlation-driven topological Kondo insulators. Yet, obtaining direct spectroscopic evidence for a d-electron HF system has been elusive to date. Here, we report the observation of Kondo lattice behavior in an antiferromagnetic metal, FeTe, via ARPES, scanning tunneling spectroscopy, and transport property measurements. The Kondo lattice behavior is represented by the emergence of a sharp quasiparticle and Fano-type tunneling spectra at low temperatures. The transport property measurements confirm the low-temperature Fermi liquid behavior and reveal successive

coherent-incoherent crossover upon increasing temperature. We interpret the Kondo lattice behavior as a result of hybridization between localized Fe $3d_{xy}$ and itinerant Te $5p_z$ orbitals. Our observations strongly suggest unusual cooperation between Kondo lattice behavior and long-range magnetic order. Some parts of this chapter are adopted from the previous work [1].

3.1 Backgrounds

3.11 Kondo effect

The Kondo effect describes the scattering of conduction electrons via magnetic impurities at low temperatures. The phenomenon was first discovered in 1936, showing a minimum in resistivity of Au [2]. Prof. Jun Kondo derived a solution using perturbation theory [3]. The dependence of the resistivity on temperature can be written as

$$\rho(T) = \rho_0 + aT^2 + c_m \ln\frac{\mu}{T} + bT^5$$

where ρ_0 is residual resistivity and aT^2 is the contribution from Fermi liquid behavior, $c_m \ln\frac{\mu}{T}$ is from Kondo scattering, and bT^5 is from lattice vibrations. The heart of the Kondo effect is random scattering by magnetic impurities, leading to an increase in resistivity and incoherence in electronic structures.

3.12 Kondo lattice

If magnetic impurities in the Kondo problem are placed periodically, the periodicity can develop coherency via Kondo interaction [4]. This is called as Kondo lattice, where local magnetic moments are located at each site of a lattice. The demonstrative system

having a Kondo lattice is the f-electron system, where local magnetic moments are intrinsically formed from a partially filled f-electron shell. The resultant feature of the Kondo lattice enhanced electron mass since the newly formed quasiparticles have significantly enhanced mass due to hybridization with localized bands. Thus, the Sommerfeld coefficients of such materials are enhanced by two- or three-times magnitude compared to their non-magnetic counterpart [5].

3.2. Introduction

Most heavy fermion materials are f-electron systems, according to previous experimental and theoretical studies [4,6,7]. Recently, Kondo interactions have been proposed to host HF states in d-electron systems as well [8-11]. It is important to study HF states in d-electron materials since the diversity of d-electron systems may lead to exotic Kondo interactions, such as topological Kondo insulating states [12] or cooperation between Kondo lattice behavior and long-range magnetism [13]. Thus, the novelty calls for new studies to find HF in d-electron material groups.

FeTe can be a candidate material to observe d-electron HF states. Its electron correlation is the strongest among iron-based superconductors (IBSCs) [14]. The magnetic ground state is known to be bicollinear antiferromagnetism (BAFM) with a large magnetic moment of 2.1 μB, implying the local nature of the magnetism [14]. The Sommerfeld coefficient of FeTe is reported to be 31.4 mJ/(K2·mol), indicating a heavy effective mass of the system [15]. This value is much larger than that of other iron

chalcogenides; FeS and FeSe for instance have 3.8 and 6.9 mJ/(K^2·mol), respectively [16,17].

In addition to these HF-related properties, other transport properties suggest the existence of strong spin-electron interaction. The temperature-dependent resistivity exhibits a drastic change at the Néel temperature (T_N). It shows an insulating behavior above T_N, but a metallic behavior below T_N [18]. The aforementioned properties of FeTe imply that the local magnetic moment significantly affects the electronic structure. Thus, electronic structure studies on the HF state of FeTe can unveil its origin and how it couples with magnetism.

In this chapter, we report on a comprehensive study on FeTe using angle-resolved photoemission spectroscopy (ARPES), transport property measurements and scanning tunneling spectroscopy (STS). We observe a hallmark of an HF behavior in ARPES spectra: a sharp quasiparticle peak (QP) near the Γ point and its strong temperature dependence. The observed QP is attributed to Kondo hybridization between Fe $3d_{xy}$ and Te $5p_z$. The Kondo hybridization scenario is further supported by STS results, showing the Fano line shape and narrow hybridization gap. In this picture, the recovery of metallic behavior in the low-temperature region is due to the emergence of the strong QP around the Γ point. We also conducted a Heisenberg model calculation, suggesting the Kondo interaction may be responsible for the emergence of BAFM in FeTe. These results provide a unified perspective that the Kondo interaction determines the exotic physical and magnetic properties in FeTe.

3.3 Methods

3.3.1 ARPES measurements

High-resolution ARPES measurements were performed with a home lab-based laser ARPES system equipped with a 10.897 eV laser (UV-2 from Lumeras) and a time-of-flight analyzer (ARTOF 10k from Scienta Omicron) [19]. Photon energy-dependent ARPES measurements were performed at BL-21B1 of the National Synchrotron Radiation Research Center (NSRRC). All ARPES measurements were conducted with p-polarized light. Overall energy resolution for the laser ARPES and photon energy dependent ARPES measurements was set to be 2 and 14 meV, respectively. The temperature dependent measurements were conducted upon cooling, starting from 80 K. The photon energy-dependent measurements were conducted at 15 K.

3.3.2 Transport measurements

The resistivity and heat capacity measurements were carried out with a Physical Property Measurement System (PPMS from Quantum Design). The resistivity and Hall coefficient measurement was conducted in a standard 4-probe and Hall bar geometry, respectively.

3.3.3 Scanning tunneling microscopy measurements

STM experiments have been performed using a home-built low-temperature STM operating at 4.3 K or 80 K. The FeTe single crystal precooled to 15 K was cleaved in the ultra-high vacuum condition. The cleaved FeTe sample was immediately inserted into the STM head. A PtIr tip is used for the measurements, and the tip quality is checked by the surface interference pattern on Cu(111). To acquire *dI/dV* spectra, a standard lock-in technique was used with a modulation frequency of f = 718 Hz.

3.3.4 Band structure simulation

The band structure simulation with a toy model is conducted to simulate ARPES results with finite k_z broadening where a strongly k_z-dispersive band is hybridized with a localized band. The simulation is based on a two-band model with a finite hybridization. The Hamiltonian is defined as

$$H = \begin{pmatrix} E_p(\vec{k}) & \Delta \\ \Delta & E_d(\vec{k}) \end{pmatrix},$$

where

$$E_p(\vec{k}) = 5t\left(\frac{k_x}{\pi}\right)^2 + 100t\cos(k_z) - \mu,$$

$$E_d(\vec{k}) = -\frac{t}{200}\left(\frac{k_x}{\pi}\right)^2 - t\cos(k_z) - \mu,$$

$$\Delta = 10t.$$

t is the energy scale of the hopping parameter and μ is the chemical potential of the system which is set arbitrarily. The basis of each axis is p, d orbitals, respectively. The in-plane dispersion is defined as parabolic and out-of-plane dispersion is defined as a cosine function. The dispersion parameter is based on the DFT calculation and ARPES results on $FeTe_{1-x}Se_x$[20, 22-24]. The diagonalized band structures are projected onto the (001) surface and plotted in Fig. 5f. For Fig. 5e, only $E_p(\vec{k})$ is plotted to simulate the ARPES data at 80 K where hybridization does not occur. The blue and red intensity in Fig. 5 denotes the orbital character of p_z and d_{xy}, respectively.

3.4 Results

3.4.1 Transport properties

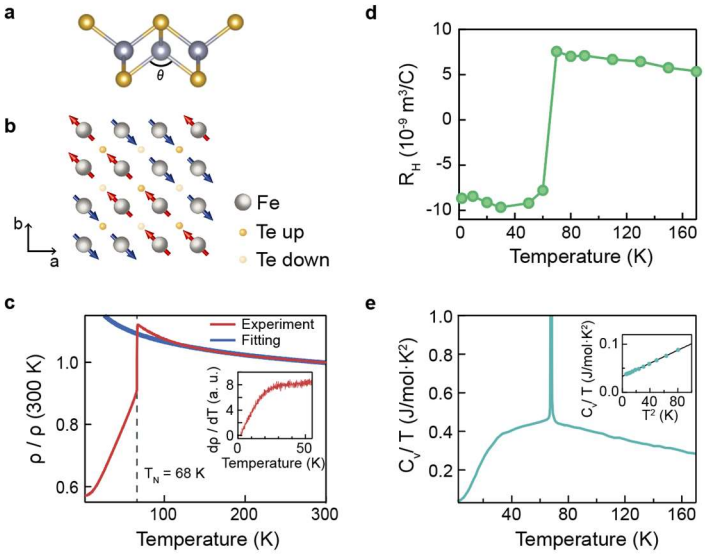

Figure. 3.1. Crystal structure and transport results of FeTe. (a) Crystal structure of FeTe. (b) Spin configuration of bicollinear antiferromagnetic (BAFM) state in FeTe. (c) Temperature-dependent resistivity. The red curve is the experimental data while the blue curve is the fitting result of the logarithmic function (a+b log(T)) of the data between 120 K and 300 K. Inset shows the temperature-derivative of the resistivity. (d) Temperature-dependent Hall coefficient. (e) Temperature-dependent C_v/T. Inset shows C_v/T vs T^2 plot in the low-temperature region. The black solid line in the inset is the fit result of $C_v/T = \gamma + \beta T^2$.

FeTe has the simplest crystal structure among the IBSCs as shown in Fig. 3.1a. Compared to other similar iron chalcogenide systems of FeSe and FeS, FeTe has a distinctive bonding angle value θ shown in Fig 3.1(a). More specifically, Te atom is pushed away from the Fe plane due to its large atomic size and, as a result, FeTe has a

small θ value [20]. This aspect of the crystal structure leads to localization of the Fe $3d_{xy}$ band as the d_{xy} orbital is confined in the Fe plane. A recent ARPES study showed a complete loss of coherent spectral weight in the d_{xy} band in FeTe, indicating a strong localization in the band [14,21]. The magnetic ground state of FeTe is bicollinear antiferromagnetism (BAFM) as shown in Fig. 1b below a Néel temperature of near 70 K [18]. It is noteworthy that among IBSCs, only FeTe exhibits BAFM. The ordering vector of BAFM in FeTe is (π/2, π/2) (1-Fe unit cell) while that of conventional AFM shown on other IBSCs is (π, 0) [22].

Transport properties show a close relationship with magnetic properties. The temperature-dependent resistivity in Fig. 1c shows insulating behavior above T_N. We find the temperature dependence follows a logarithmic behavior of -ln(T). On the other hand, it abruptly recovers a metallic behavior below T_N. More specifically, it shows a Fermi liquid behavior below 15 K with a T^2 dependence resistivity, and a T-linear behavior between 30 K and 70 K. These T-dependent behaviors indicate the existence of coherent-incoherent crossover around 15 K (see the inset of Fig. 1c and Supplementary Information). It is also noteworthy that the resistivity shows a minimum at around 2.2 K (see Supplementary Information for the corresponding data and discussion). The Hall coefficient, as well as the resistivity, shows a drastic change at T_N. The Hall coefficient changes hole dominant ($T > T_N$) to electron dominant ($T < T_N$) at T_N as can be seen in Fig. 3.1d. The crossover behavior seen in the resistivity data can be also found in the heat capacity data in Fig. 3.1e; C_v/T deviates from T^2 behavior around 15 K (see Supplementary Information for the determination of the deviation temperature). Further

analysis shows that the Sommerfeld coefficient extracted from the heat capacity is 33.4 mJ/mol·K^2 (see the inset of Fig. 3.1e). It is much larger than that of other iron chalcogenides. For instance, it is 3.8 and 6.9 mJ/mol·K^2 for FeS and FeSe, respectively [16,17].

3.4.2 Electronic structures

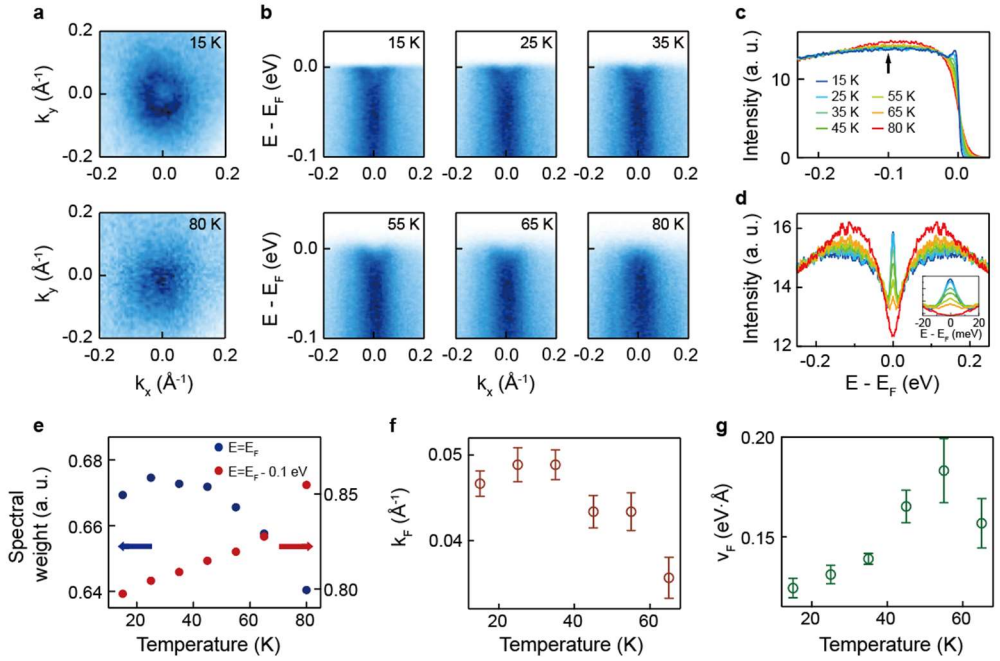

Figure 3.2. Electronic structure of FeTe. (a) Fermi surface (FS) maps from high-resolution laser-ARPES measurements, obtained at 15 and 80 K. (b) Temperature-dependent high symmetry cuts along the Γ-X direction. ARPES data were taken with 11 eV photons. (c) Energy distribution curves (EDCs) integrated within a certain momentum range ($k_x^2 + k_y^2 < (0.15\ Å^{-1})^2$). The EDCs are normalized with the integrated intensity

from an energy window of -0.25 eV < E – E_F < -0.2 eV. (d) Symmetrized EDCs of (c). Inset: enlarged view of EDCs near the Fermi level. (e) Temperature-dependent spectral weight at E = E_F and E = E_F – 0.1 eV. (f and g) Temperature-dependent Fermi momentum (k_F) and Fermi velocity (v_F), respectively, obtained from momentum distribution curve (MDC) analysis. Errors bars in (f and g) represent the fitting errors of Fermi momentum and Fermi velocity, respectively.

We turn our attention to the electronic structure of FeTe. High-resolution laser ARPES experiments were performed to track the temperature-dependent evolution of the electronic structure. The Fermi surfaces (FSs) near the Γ point shown in Fig. 3.2a exhibit significant temperature dependence as the temperature decreases from 80 K to 15 K. A single circular FS pocket is clearly observed at 15 K while it becomes a blob at 80 K. Evolution of the electronic structure can be also seen in the high symmetry cuts along the k_x-direction shown in Fig. 3.2b. It is revealed that the FS pocket observed at 15 K in Fig. 2a comes from an electron band. As the temperature increases, the electron band tends to be broadened and vanishes abruptly at 80 K.

This observed temperature dependence of the band can be more clearly seen in the temperature-dependent energy distribution curves (EDCs) plotted in Fig. 3.2c. A clear QP is observed at the lowest temperature, which comes from the electron band mentioned above. Upon increasing temperature, the QP is gradually suppressed while the spectral weight of the hump centered at -0.1 eV, indicated by an arrow in Fig. 3.2c, gradually increases. Such spectral weight transfer behavior is more pronounced in symmetrized

EDCs in Fig. 3.2d. Analysis of the spectral weight transfer behavior is depicted in Fig. 3.2e. It clearly shows that the lost QP spectral weight is transferred to the 0.1 eV hump, demonstrating that the observed temperature dependence is intrinsic. It is also noteworthy that the full width at half maximum (FWHM) of the QP obtained from a Lorentzian fitting is 7.9 meV as can be seen in the inset of Fig. 3.2d, implying remarkable heavy mass and long quasiparticle lifetime of the band.

Additional band fitting analyses provide more information about the temperature-dependent evolution of the band. We extract the Fermi momentum (k_F) and Fermi velocity (v_F) using momentum distribution curve (MDC) analysis as depicted in Figs. 3.2(f) and 3.2(g), respectively. Temperature-dependent k_F value shows that the FS pocket size tends to enlarge upon cooling. Meanwhile, v_F of the electron band decreases with the temperature. From these results, we can infer that the temperature evolution of the k_F and v_F did not result from a simple chemical potential shift. The origin of the evolution will be discussed below.

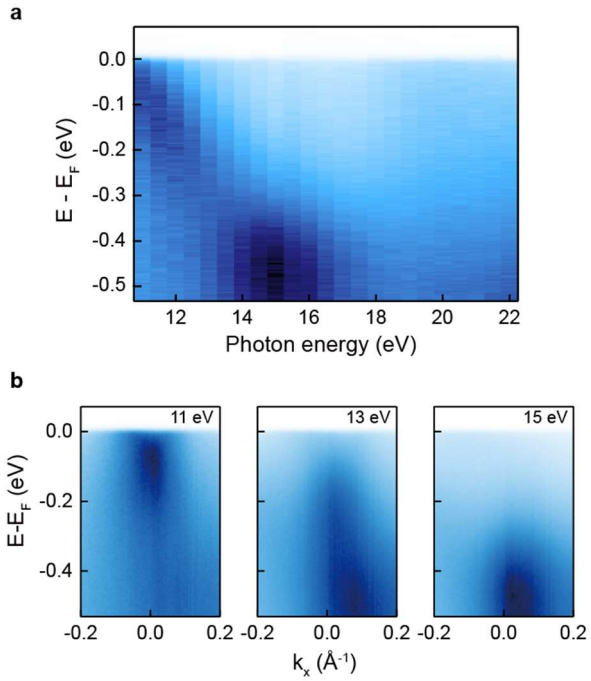

Figure 3.3. Photon energy-dependent electronic structure. (a) Photon energy-dependent electronic structure near the Γ point. (b) Photon energy-dependent high symmetry cuts along the Γ-X direction, obtained using 11, 13, 15 eV photon.

The photon energy-dependent ARPES result gives further insights into the origin of the band. As can be seen in Fig. 3.3, the electron band which is clearly visible at 11 eV has a strong k_z dispersion. As the photon energy increases, the band shifts to the higher binding energy side, and its energy scale becomes more than 0.5 eV. Considering FeTe is in the strongly correlated limit, a bandwidth of 0.5 eV far surpasses that of Fe 3d bands [20]. In addition, the photoionization cross section of Te 5p orbital is much larger than that of Fe 3d orbital at 11 eV [23]. Thus, the band observed at 11 eV is likely to be mostly from Te p_z orbital. We note that similar k_z dispersion behavior was also reported for $FeTe_{0.55}Se_{0.45}$

[24].

Considering the large dispersion of the p_z band away from E_F as shown in Fig. 3.3, the sharp QP near E_F implies that the band undergoes a strong modulation. Two scenarios may be considered for the modulation: (i) electron-bosonic mode coupling and (ii) Kondo hybridization between the itinerant and localized bands. It was claimed in a previous ARPES study on FeTe that the feature is a result of strong electron-phonon coupling, namely a polaronic behavior [25]. However, such a scenario may not explain the enlargement of the Fermi surface at low temperatures in Fig. 3.2f since an electron-boson coupling should conserve the k_F. Alternatively, one can consider a Kondo hybridization scenario which should also show a mass enhancement at low temperatures and strong temperature dependence of the QP. Therefore, it is highly desirable to have an alternative way to discern the two scenarios.

3.4.3 Fano line shape and hybridization gap

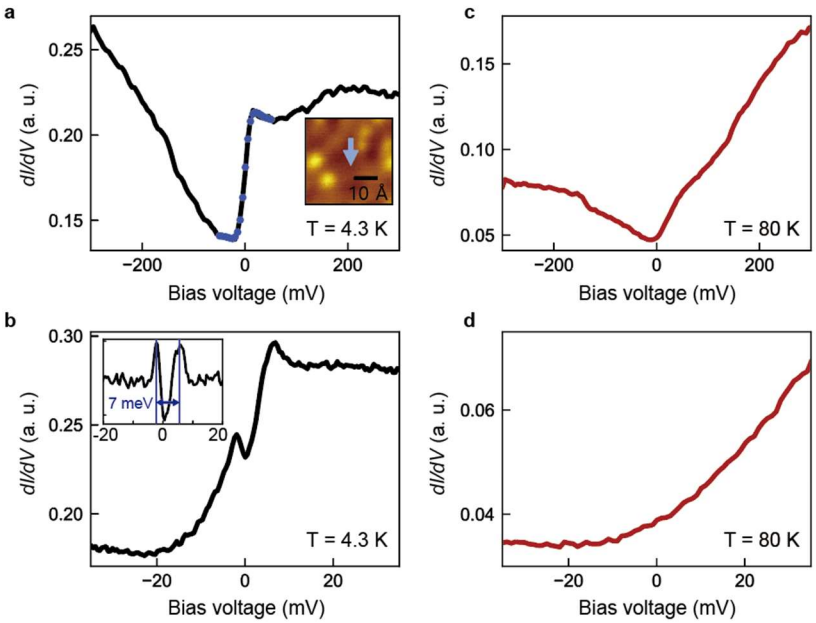

Figure 3.4. STS results on FeTe. (a) Differential conductance (dI/dV) spectrum measured on FeTe surface at 4.3 K. The blue circles represent the Fano fitting of the Kondo resonance (see Supplementary Information for the fitting parameters). The inset shows the position where the spectrum is taken. Vbias = -300 mV, I = 100 pA and Lockin-modulation V_{mod} = 5 mV_{pp}. (b) dI/dV spectrum enlarged around the Fermi energy. The inset is the spectrum after subtracting the smoothly-varying background. V_{bias} = -40 mV, I = 100 pA and V_{mod} = 500 μV_{pp}. (c) dI/dV spectra measured at 80 K. V_{bias} = -300 mV, I = 50 pA and V_{mod} = 5 mV_{pp}. (d) Zoomed-in dI/dV spectrum. Vbias = -40 mV, I = 50 pA and V_{mod} = 500 μV_{pp}.

Whether the strong renormalization of the dispersion near E_F is due to Kondo hybridization or not may be determined based on tunneling spectra. Shown in Fig.

3.4 are STS data at 4.3 and 80 K. A wide energy range scan at 4.3 K depicted in Fig. 3.4a shows an asymmetric spectrum. The spectrum is found to be well fitted with a Fano line shape as illustrated in the figure. It is well-known that tunneling spectra from a Kondo singlet state should exhibit a Fano-type resonance [13]. The Fano fit shown as blue circles in Fig. 3.4a gives a Fano line width (Γ value) of 24.1 meV, which corresponds to the Kondo temperature of about 280 K. Furthermore, a closer look of the data over a narrow energy range around E_F plotted in Fig. 3.4b shows a gap feature that is consistent with a gap expected for a Kondo hybridization scenario. We subtract the smoothly-varying background from the data and plot it in the inset. The subtracted data shows a gap with a size of about 7 meV as seen in Fig. 3.4b. In addition, it is seen that the gap feature is slightly shifted to the unoccupied side. Plotted in Figs. 3.4c and 3.4d are dI/dV spectra taken at 80 K, above T_N. The two spectra are taken over the same energy ranges as the 4.3 K data. The Kondo-related features are expected to disappear at high temperatures, which are indeed seen in the high-temperature data in Figs. 3.4c and 3.4d; the Fano behavior is weakened and the hybridization gap has disappeared. Therefore, these observations – Fano behavior and narrow gap near E_F – are clear signs of Kondo hybridization, confirming that FeTe exhibits Kondo hybridization below T_N.

3.5 Discussion

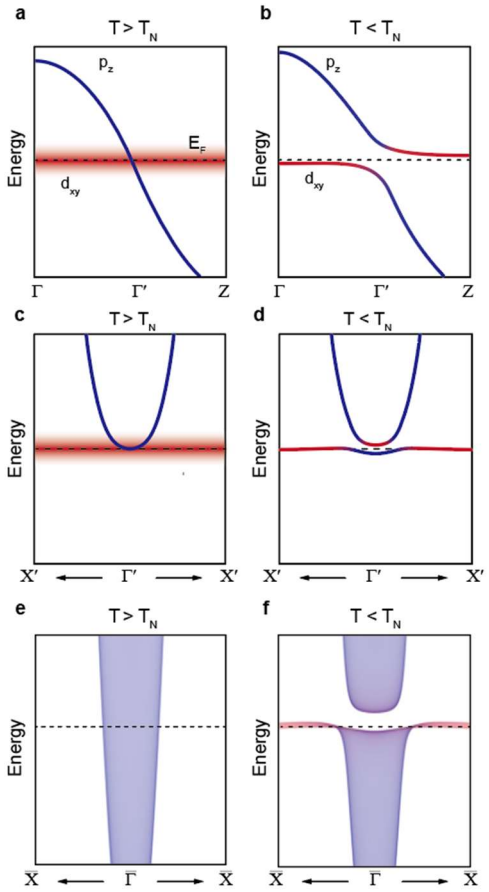

Figure. 3.5. Schematic of the Kondo hybridization scenario. (a and b) Band structure of FeTe along the Γ-Z direction (out-of-plane) above and below T_N, respectively. (c and d) Band structure of FeTe along the Γ-X direction (in-plane) above and below T_N, respectively. (e and f) Simulated band structure projected onto the (001) surface along the Γ-X direction (in-plane) above and below T_N, respectively. Blue bands denote p_z orbital, and red bands denote d_{xy} orbital.

Fully considering our comprehensive data, we argue that the electron band that emerges below T_N is a result of a Kondo hybridization between the itinerant p_z and localized d_{xy} bands. The argument is based on the fact that only the d_{xy} orbital of FeTe is in a localized state, which is a prerequisite for the Kondo effect [4,14]. Density functional theory calculations also confirm the band we measured in ARPES has Te p_z and Fe d_{xy} orbital characters (see the Appendix). Here, it is also noteworthy that the appearance of the coherence peak may be accounted for within the coherence-incoherence crossover picture in Hund's metal [26-29] as observed in some of the iron-based superconductors [26,29]. However, the Kondo hybridization picture is needed to explain the other aspects of the experimental results. Indeed, recent theoretical work proposed that the interorbital hopping in the orbital-selective Mott phase can develop a narrow quasiparticle peak near the Fermi level [30]. In this perspective, our work emphasizes the role of interorbital coupling. When the system enters the BAFM state, the p_z and d_{xy} bands start to Kondo hybridize as illustrated in Fig. 3.5; the strongly dispersive p_z band along k_z direction crosses the localized d_{xy} band, resulting in a Kondo hybridization and heavy electron band. The correlation between Kondo hybridization and BAFM is discussed later. Based on known band dispersions, we simulate the band structure with a finite hybridization between the p_z and d_{xy} band. The simulated band structures projected onto the (001) surface in Figs. 3.5e and f well coincide with ARPES results shown in Fig. 3.2b at the temperature of 80 K and 15 K, respectively. In addition, the narrow gap in the unoccupied side at low temperature and its disappearance at high temperature in the STS data directly support the band diagram illustrated in Fig. 3.5f and e, respectively. The details of the

simulation are described in the Methods section. The Kondo hybridization scenario is further supported by previous inelastic neutron scattering measurements on FeTe: the study reported that the local magnetic moment of FeTe is S = 1 at 10 K but it unexpectedly grows to S = 3/2 at 300 K, suggesting low-temperature Kondo screening of the local moments by itinerant electrons [31]. Note that the d_{xy} band is not visible near the Fermi level since d_{xy} band is strongly localized and thus its spectral weight near the Fermi level is mostly transferred to the high binding energy region and the photoionization cross section of Te 5p orbitals far surpass that of Fe 3d orbitals at 11 eV photon.

The observed heavy electron band resulting from Kondo hybridization can address the unique transport properties of FeTe: (i) recovery of metallic behavior below T_N, (ii) sudden sign change in the Hall conductivity at T_N, and (iii) emergent Fermi liquid behavior at low temperature. First, the recovery of metallic behavior can be understood through the emergence of the sharp and strong QP at the Fermi level near the Γ point at T_N; the transport properties are dominated by the QP. The emergence of the electron QP below T_N can also explain the sign change in the Hall conductivity, from hole dominant ($T > T_N$) to electron dominant ($T < T_N$). A previous study reported that recovery of the metallic behavior and Hall coefficient change may be related to the formation of pseudogap near the Brillouin zone corner33. However, their observation is not enough to explain the abrupt change in the resistivity and Hall conductivity. It is also noteworthy that such a strong QP and its strong temperature dependence are only observed at the Γ point (see Appendix for the temperature dependent ARPES results on the X point pocket.). Thus, we believe the FS near the Γ point, which exhibits a sudden change at T_N,

dominates transport properties. Finally, the sharp QP bandwidth of 7.9 meV indicates a long quasiparticle lifetime, indicating that FeTe is in a Fermi liquid regime at low temperatures. This observation is consistent with the unique transport results and enhanced Sommerfeld coefficient of FeTe. We note that recent ARPES and STS studies on $CeRh_2Si_2$ and SmB_6 reported significantly different Kondo properties at the surface and in the bulk [32-34]. In such cases, considering the surface sensitivity of ARPES and STS, the Kondo-related properties of FeTe observed via ARPES and STS can be different from those of transport measurements. However, the crystal structure of FeTe is quasi-two-dimensional, which is distinct from $CeRh_2Si_2$ and SmB_6. This feature might be the reason for the consistency in the Kondo properties of FeTe observed by ARPES and transport measurements.

The overall temperature dependence of electronic structures and transport properties are well explained within the Kondo lattice scenario. In the paramagnetic (PM) state, FeTe is in the Kondo scattering regime, consistent with the logarithmic resistivity and estimated Kondo temperature from Fano line width (see Appendix for detailed parameters). From the electronic structure point of view, the strong scattering in the Kondo scattering regime results in breakdown of a well-defined quasiparticle, which in turn leads to loss of spectral weight and its transfer to a higher binding energy region. Thus, the hump structure is the incoherent counterpart of the QP, supported by the spectral weight transfer as shown in Fig. 3.2e. The broadened but persistent Fano line shape at 80 K also indicates the system is still in the Kondo scattering regime, while strongly suppressed coherency above T_N leads to the loss of the QP. On the other hand,

when the system enters the BAFM state, low-temperature behaviors of a Kondo lattice emerge: a sharp quasiparticle peak in the electronic structure induced by Kondo hybridization as well as a Fermi liquid behavior (T_2 dependence) at low temperature followed by a coherent-incoherent crossover in resistivity. Based on these facts, we may address the unique feature of the Kondo lattice behavior in FeTe; low-temperature Kondo lattice behaviors in FeTe suddenly set in at the onset of BAFM as evidenced by the abrupt drop in the resistivity and sudden emergence of QP at T_N. This drastic shift of the system to the low-temperature Kondo lattice regime at the onset of the BAFM suggests a possible positive correlation between BAFM and Kondo lattice behavior in FeTe.

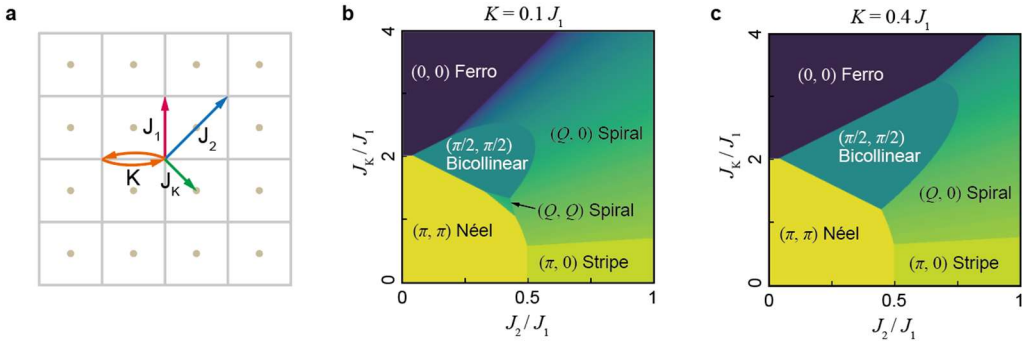

Figure 6. Magnetic phase diagram of FeTe from Heisenberg model. (a) Definition of the Heisenberg model parameters. Grey solid lines denote the prime square lattice, whereas brown dots denote sublattice. J_1 and J_2 are nearest-neighbor (NN) and next nearest-neighbor (NNN) exchange interactions, respectively, on the prime lattice. J_K denotes NN exchange interaction between the prime lattice and sublattice. K is the NN biquadratic exchange interaction. (b and c) Magnetic phase diagram calculated from the model Hamiltonian (Eqn. 1) with K = 0.1 and 0.4, respectively.

To reveal the underlying mechanism of the positive correlation between BAFM and Kondo lattice behavior in FeTe, we conducted a Heisenberg model calculation with an additional Fe-Te exchange interaction. Based on the established two-neighbor Heisenberg model with the biquadratic term (J_1-J_2-K model) on a prime square lattice, we additionally introduce a centered sublattice as shown in Fig. 3.5a to take into account the Fe-Te interaction (defined as J_K hereafter). We define the J_1-J_2-J_K-K model on the combined lattice as

$$H = J_1 \sum_{<i,j>} \vec{S_i} \cdot \vec{S_j} - K \sum_{<i,j>} \left(\vec{S_i} \cdot \vec{S_j}\right)^2 + J_2 \sum_{\ll i,j \gg} \vec{S_i} \cdot \vec{S_j} + J_K \sum_{<i,k>} \vec{S_i} \cdot \vec{s_k}$$

where J_1 and J_2 are nearest-neighbor (NN) and next nearest-neighbor (NNN) exchange interactions on the prime lattice, respectively, and K is the NN biquadratic exchange interaction, while J_K is the NN interaction between prime lattice and sublattice as described in Fig. 3.6a. i and j are indices for the prime lattice, and k is the sublattice index.

We solved the J_1-J_2-J_K-K model for various K values and obtained the corresponding magnetic phase diagram in Fig. 3.6b and c. For a small J_K, the model well reproduces (π, 0) stripe phase in iron pnictides. As J_K grows, ($\pi/2$, $\pi/2$) BAFM starts to be stabilized and spans the phase diagram over a wide range of K (see Supplementary Information for an extended phase diagram.). Within the J_K-induced BAFM scenario, the sublattice (Te atom for FeTe) should be also spin-polarized accordingly. We note that previous spin-polarized scanning tunneling microscopy measurements on FeTe revealed that Te atoms are also spin-polarized in the BAFM state. These results suggest that J_K, an exchange interaction

between Fe and Te, may play a crucial role in stabilizing the BAFM in FeTe. This J_K-induced BAFM scenario thus explains the positive correlation between Kondo lattice behavior and BAFM since the Kondo lattice behavior and BAFM share the same origin, J_K. The positive correlation between long-range magnetism and Kondo lattice state is reminiscent of the underscreened Kondo lattice model in UTe and $UCu_{0.9}Sb_2$, where a local magnetic moment of S = 1 is not fully screened by itinerant electrons. Likewise, the local moment of S = 3/2 in FeTe at 300 K is not fully screened, resulting in a residual local moment of S = 1 at 10 K, suggesting a possible analogy with the underscreened Kondo lattice model.

We find the J_1-J_2-J_K-K model has further implications. It was previously reported that an unexpected ferromagnetic (FM) state emerges under hydrostatic pressure [35]. A transition from BAFM to FM occurs in our calculated magnetic phase diagram if J_K is further increased. Note that previously proposed Heisenberg models had to employ the third nearest-neighbor exchange interaction (J_3) to account for the BAFM in FeTe, but could not predict the FM phase. In other words, the inclusion of J_K may be the key to understanding the magnetic order in FeTe.

3.6 Conclusion and remarks

Recently, there have been numerous studies reporting that orbital-selectiveness is a prominent ingredient to make physics diverse in correlated d-electron multiorbital systems. In particular, while the orbital-selective Mott phase itself is an intriguing

phenomenon, another important aspect is that materials with orbital-selective Mott phase are vulnerable to Kondo hybridization and thus may result in a new type of HF state. We thus suppose that the local magnetic moment formed in the orbital-selective Mott phase critically affects the physical and magnetic properties of FeTe via Kondo interaction. Our results shed light on the role of the local magnetic moments in correlated d-electron multiorbital systems.

References

[1] Y. Kim *et al.*, arXiv preprint arXiv:2203.06432 (2022).

[2] W. De Haas and G. Van Den Berg, Physica **3**, 440 (1936).

[3] J. Kondo, Progress of theoretical physics **32**, 37 (1964).

[4] S. G. Stewart, Reviews of Modern Physics **56**, 755 (1984).

[5] P. Coleman, arXiv preprint cond-mat/0612006 (2006).

[6] N. Mathur, F. Grosche, S. Julian, I. Walker, D. Freye, R. Haselwimmer, and G. Lonzarich, Nature **394**, 39 (1998).

[7] S. Wirth and F. Steglich, Nature Reviews Materials **1**, 1 (2016).

[8] Y. Wu, D. Zhao, A. Wang, N. Wang, Z. Xiang, X. Luo, T. Wu, and X. Chen, Physical Review Letters **116**, 147001 (2016).

[9] M. Kim *et al.*, arXiv preprint arXiv:2102.09760 (2021).

[10] D. Zhao *et al.*, Physical Review B **97**, 045118 (2018).

[11] A. Shimoyamada *et al.*, Physical review letters **96**, 026403 (2006).

[12] K.-J. Xu *et al.*, Proceedings of the National Academy of Sciences **117**, 15409 (2020).

[13] Y. Zhang *et al.*, Science advances **4**, eaao6791 (2018).

[14] Z. P. Yin, K. Haule, and G. Kotliar, Nat Mater **10**, 932 (2011).

[15] P. Maheshwari, V. R. Reddy, and V. Awana, Journal of Superconductivity and Novel Magnetism **31**, 1659 (2018).

[16] J. Xing, H. Lin, Y. Li, S. Li, X. Zhu, H. Yang, and H.-H. Wen, Physical

Review B **93** (2016).

[17] L. Wang, F. Hardy, T. Wolf, P. Adelmann, R. Fromknecht, P. Schweiss, and C. Meingast, physica status solidi (b) **254** (2017).

[18] J. Jiang, C. He, Y. Zhang, M. Xu, Q. Q. Ge, Z. R. Ye, F. Chen, B. P. Xie, and D. L. Feng, Physical Review B **88** (2013).

[19] Y. He *et al.*, Review of Scientific Instruments **87**, 011301 (2016).

[20] M. Yi, Y. Zhang, Z.-X. Shen, and D. Lu, npj Quantum Materials **2** (2017).

[21] J. Huang *et al.*, Communications Physics **5**, 1 (2022).

[22] T. J. Liu *et al.*, Nat Mater **9**, 716 (2010).

[23] X. L. Peng *et al.*, Physical Review B **100** (2019).

[24] Z. Wang *et al.*, Physical Review B **92** (2015).

[25] Z. K. Liu *et al.*, Phys Rev Lett **110**, 037003 (2013).

[26] H. Miao *et al.*, Physical Review B **94**, 201109 (2016).

[27] Z. Yin, K. Haule, and G. Kotliar, Physical Review B **86**, 195141 (2012).

[28] M. Yi *et al.*, Nature communications **6**, 1 (2015).

[29] M. Yi *et al.*, Physical review letters **110**, 067003 (2013).

[30] F. B. Kugler and G. Kotliar, Physical review letters **129**, 096403 (2022).

[31] I. A. Zaliznyak, Z. Xu, J. M. Tranquada, G. Gu, A. M. Tsvelik, and M. B. Stone, Physical review letters **107**, 216403 (2011).

[32] G. Poelchen *et al.*, npj Quantum Materials **5**, 1 (2020).

[33] S. Patil *et al.*, Nature communications **7**, 1 (2016).

[34] L. Jiao, S. Rößler, D. Kim, L. Tjeng, Z. Fisk, F. Steglich, and S. Wirth,

Nature communications **7**, 1 (2016).

[35] K. Mydeen *et al.*, Phys Rev Lett **119**, 227003 (2017).

Chapter 4

Strongly anisotropic superconducting gap symmetry in Fe(Te,Se)

Superconducting gap symmetry is one of the most intrinsic parameters determining the properties of superconducting materials. In particular, recent advances in quantum information and computing technology urge to find and realize stable superconducting devices, which can be realized by using topological superconductors. Since the topological superconductors can be realized in odd-parity superconducting gap symmetry or frustration of two independent superconducting gap symmetry, finding and measuring new types of superconducting gap symmetry have been an important task. In this chapter, the superconducting gap symmetries of Fe(Te,Se) compounds are demonstrated by using the developed ultra-high-resolution laser-based ARPES system. The results show Fe(Te,Se) compounds show strong anisotropic gap symmetry near Te end. Considering the conventional s±wave gap condition is broken near Te end, the anisotropic gap symmetry may be an indication of new superconducting gap symmetry such as nodal s, which was demonstrated in hole-doped iron pnictides.

4.1 Backgrounds

4.1.1 Superconducting gap symmetry of unconventional superconductors

Unconventional superconductivity is a superconductivity that deviates from BCS's assumption. The BCS's assumption is i) phonon-mediated, ii) isotropic s-wave, and iii) weak coupling [1]. Unconventional superconductors show different behavior from the aforementioned BCS's assumption. The prime example is spin fluctuation-mediated superconductivity [2]. The spin fluctuation is known to mediate superconductors. Since the coupling potential of spin fluctuations is positive, an additional condition to overcome detrimental Coulomb repulsion is imposed for the emergence of the superconductivity; the integration of the superconducting gap over the whole Brillouin zone should be zero. This can be understood by the following argument. The wavefunction of electrons can be written as $\psi(r) = \sum_k \psi_k e^{ik\cdot r}$. Since on-site Coulomb repulsion is strong ($V(0) \gg 1$), the wavefunction should satisfy the following condition to save the potential energy.

$$\psi(0) = \sum_k \psi_k e^{ik\cdot 0} = 0$$

In weak coupling limit, $\psi_k \sim \Delta_k$. Hence, $\sum_k \Delta_k = 0$. This condition should be considered for positive coupling potential (note that the coupling potential of phonons is negative, which does not need the aforementioned condition.). Since iron-based superconductors are though to be mediated by spin fluctuations, the condition should also be considered in iron-based superconductors [3].

Iron-based superconductors generally show s±-wave superconductivity. The hole pocket near the Γ point and the electron pocket near the M point have opposite superconducting phases. However, it is reported that some iron-based superconductors show different superconducting gap symmetry other than s±-wave superconductivity [4-6].

4.1.1 Deviation of s±-wave condition in Fe(Te,Se)

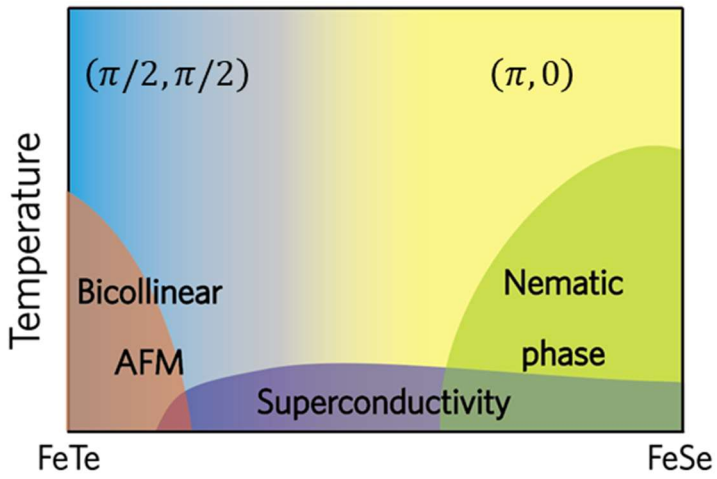

Fig. 4.1 Phase diagram of Fe(Te,Se). Blue-shaded region denotes the (π/2, π/2) spin fluctuation-dominated region, whereas the yellow-shaded region denotes the (π, 0) spin fluctuation-dominated region

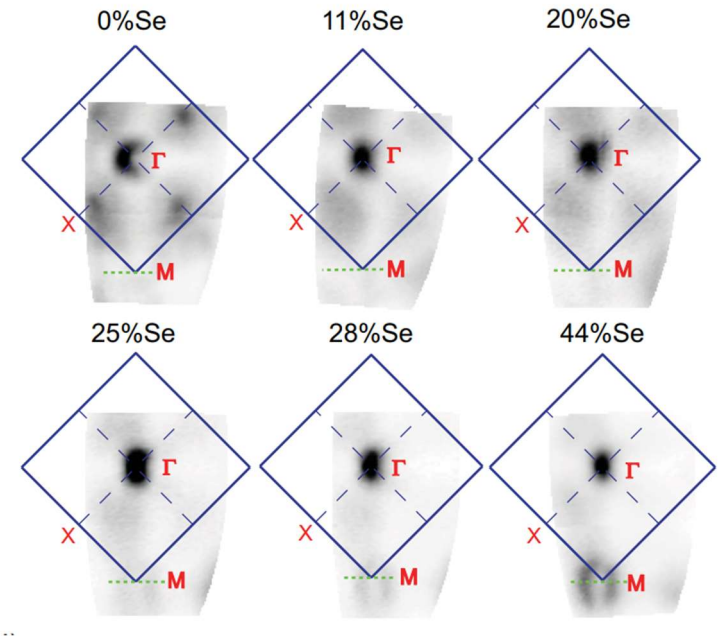

Figure. 4.2 Fermi surface of Fe(Te,Se) measured by ARPES [7].

In Te end, the s±-wave condition is broken in two ways: i) the dominant spin fluctuation is (π/2, π/2) as can be seen in Fig. 4.1 [8]; ii) the M point pocket disappears as shown in Fig. 4.2. Considering these facts, it can be expected that the Fe(Te,Se) compounds exhibit possible deviation from s±-wave superconductivity.

4.2 Experimental details

High-quality Fe(Te,Se) single crystals were grown using the modified Bridgman method. Stoichiometric, electric, and magnetic properties were characterized by using scanning electron microscopy with energy dispersive X-ray spectroscopy (SEM-EDX), a

physical property measurement system (PPMS), and a magnetic property measurement system (MPMS), respectively. ARPES measurements were performed with a lab-based system using a p-polarized laser photon source ($h\nu$ = 21.2 eV). Spectra were acquired using ARTOF 10k electron analyzers with energy resolutions of 1 meV. Samples were cleaved *in situ* at T = 10 K and measured in an ultrahigh vacuum better than 5×10^{-11} Torr.

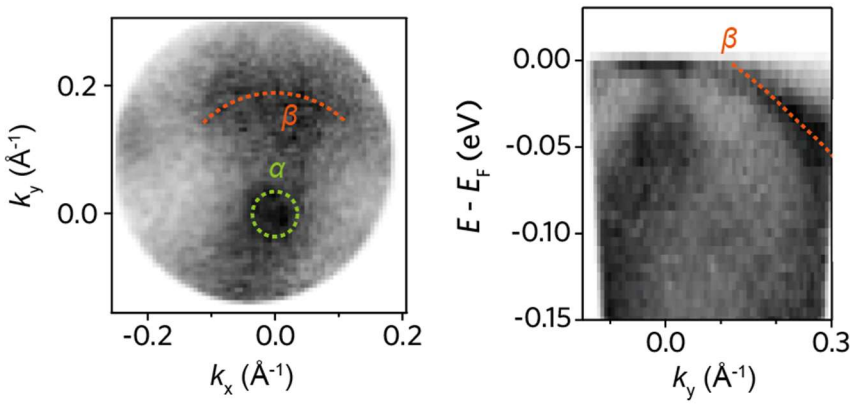

Figure 4.3 Electronic structures of $FeTe_{0.8}Se_{0.2}$. (a) Fermi surface of $FeTe_{0.8}Se_{0.2}$. (b) high-symmetry cut along the Γ-X line near the Γ point.

4.3 Results and Discussion

4.3.1 Basic electronic structure

The Fermi surface pocket of $FeTe_{0.8}Se_{0.2}$ shown in Fig. 4.3.(a) shows the two pockets. The inner/outer pocket (α/β band) corresponds to $d_{xz/yz}$ band, respectively. Due to the matrix element effect, only part of the β band is visible. The high symmetry cut along the k_y-direction is shown in Fig. 4.3(b). The β shows clear dispersion. The subsequent superconducting gap measurement is performed at the β band.

4.3.2 Superconducting gap structures

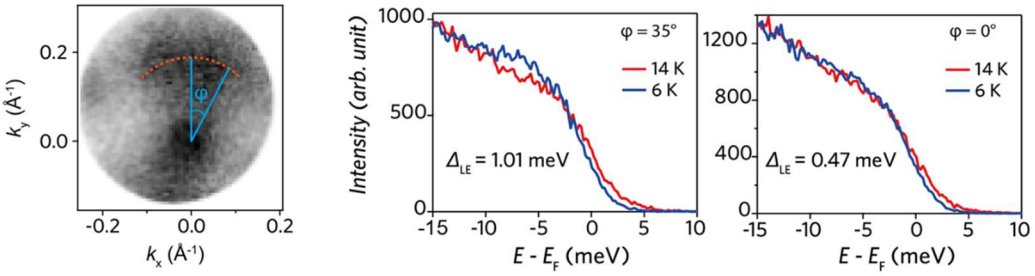

Figure 4.4 Anisotropic superconducting gap structure of $FeTe_{0.8}Se_{0.2}$

The superconducting gap of $FeTe_{0.8}Se_{0.2}$ as a function of the azimuthal angle is shown in Fig. 4.4. The superconducting gap is extracted by fitting the shift of the leading edge. The extracted gap shows quite anisotropic depending on the azimuthal angle. The minimum anisotropy is more than two times, which is much more than the reported value in $FeTe_{0.55}Se_{0.45}$. The overall azimuthal angle-dependent gap structure is shown in Fig. 4.5. The gap structure shows strongly anisotropic features.

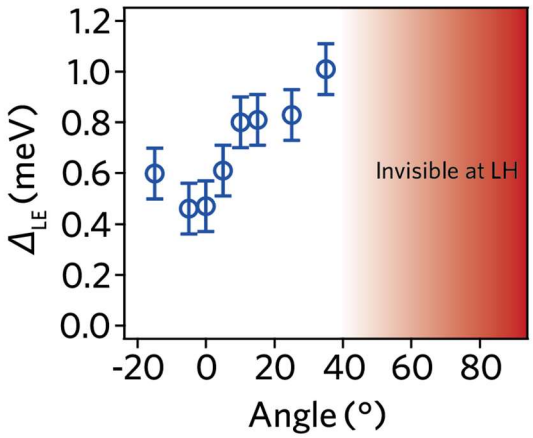

Figure 4.5 Azimuthal angle-dependent superconducting gap in $FeTe_{0.8}Se_{0.2}$

Considering the broken s±-wave condition, the superconducting gap symmetry might deviate from the s±-wave condition as in hole-doped iron pnictides. The deviation in hole-doped iron pnictide results in a new type of superconducting order parameter, which is called as nodal s-wave superconductivity. In light of the strongly anisotropic superconducting gap structure, along with broken s±-wave condition, the nodal s-wave can be one possible candidate for the superconducting order parameter in $FeTe_{0.8}Se_{0.2}$. The further systematic doping dependent study can discern the superconducting gap evolution of Fe(Te,Se) compounds. In addition, the polarization dependent measurement such as LCP+RCP can avoid the matrix element effect, which enables the extraction of the superconducting gap structure over the whole Brillouin zone.

4.4 Conclusion

Considering recent interests in topological superconductivity for further application in quantum information and computing, finding a new type of superconducting order parameter became an important task. The degeneracy of two independent superconducting states can lead to spontaneous breaking of time-reversal symmetry, i.e. *s+is* in hole doped iron pnictidies [9,10]. Likewise, Fe(Te,Se) may be another candidate that can host a new type of the superconducting order parameter. In light of the proposed topological superconductivity in $FeTe_{0.55}Se_{0.45}$, the Fe(Te,Se) compounds may be a novel platform containing multiple topological superconductivity.

References

[1] L. N. Cooper, Physical Review **104**, 1189 (1956).

[2] P. Monthoux, D. Pines, and G. Lonzarich, Nature **450**, 1177 (2007).

[3] R. M. Fernandes, A. V. Chubukov, and J. Schmalian, Nature Physics **10**, 97 (2014).

[4] T. Ong, P. Coleman, and J. Schmalian, Proc Natl Acad Sci U S A **113**, 5486 (2016).

[5] V. Borisov, R. M. Fernandes, and R. Valenti, Phys Rev Lett **123**, 146402 (2019).

[6] X. Liu, R. Tao, M. Ren, W. Chen, Q. Yao, T. Wolf, Y. Yan, T. Zhang, and D. Feng, Nat Commun **10**, 1039 (2019).

[7] Z. K. Liu *et al.*, Physical Review B **92** (2015).

[8] T. J. Liu *et al.*, Nat Mater **9**, 716 (2010).

[9] V. Grinenko *et al.*, Nature Physics **16**, 789 (2020).

[10] V. Grinenko *et al.*, Nature Physics **17**, 1254 (2021).

Chapter 5

Deep learning-based statistical noise reduction method for ARPES data

In spectroscopic experiments, data acquisition in multi-dimensional phase space may require long acquisition time, owing to the large phase space volume to be covered. In such a case, the limited time available for data acquisition can be a serious constraint for experiments in which multidimensional spectral data are acquired. In this chapter, taking angle-resolved photoemission spectroscopy (ARPES) as an example, we demonstrate a denoising method that utilizes deep learning as an intelligent way to overcome the constraint. With readily available ARPES data and random generation of training datasets, we successfully trained the denoising neural network without overfitting. The denoising neural network can remove the noise in the data while preserving its intrinsic information. We show that the denoising neural network allows us to perform a similar level of second-derivative and line shape analysis on data taken with two orders of magnitude less acquisition time. The importance of our method lies in its applicability to any multidimensional spectral data that are susceptible to statistical noise. Some part of this chapter is adopted from the previous work [1].

5.1 Introduction

Advances in a spectroscopic technique often accompany an increase in the dimension the experimental technique can cover, allowing for more comprehensive data. An excellent example of this is ARPES. A modern-day hemispherical analyzer can take two-dimensional energy/momentum space data, whereas a time-of-flight analyzer can cover a three-dimensional energy/momentum space at a time [2-5]. In addition, the recently developed momentum-resolved photoemission electron microscopy (k-PEEM) can investigate three-dimensional momentum/energy space as well as two-dimensional real space [5,6]. These advances in the analyzer technique allow for new information and thereby facilitate new discoveries. An important issue with the aforementioned developments in ARPES is that acquisition of multidimensional data has a fundamental constraint. Owing to the much increased phase space volume to be covered, taking multidimensional data necessarily requires a much longer acquisition time to get the same signal-to-noise ratio (SNR) level [7]. Increasing the light intensity may not be a solution as, in addition to its own limit, high-intensity light can bring in new issues such as detector non-linearity [5,8] or space-charge problem [9,10]. Considering the fact that a fresh surface often has a certain lifetime for adequate ARPES [5,11], this constraint in the acquisition time should be a serious limitation in multidimensional measurements. In fact, the situation also applies to other spectroscopic techniques that acquire multidimensional data. In such a case, the time constraint often affects decision making in real experiments. Therefore, development of a new methodology to overcome the time constraint is highly

desired to fully exploit the capability of advanced spectroscopic techniques.

One way to alleviate the limitation is denoising the obtained spectral data. Since the SNR is generally proportional to the square root of the total count, majority of the measurement time is spent on reducing the noise. Thus, if the noise of spectral data can be removed with the intrinsic information preserved, the data acquisition time can be drastically reduced. A conventional way to reduce the noise is the Gaussian smoothing method, exploiting the high-frequency nature of the noise. The Gaussian smoothing is widely used, especially for derivative analyses, such as second-derivative or curvature methods, since differentiation highlights the high-frequency signal and is thus vulnerable to the noise [12]. However, the Gaussian smoothing inevitably blurs data, resulting in loss of the intrinsic information.

Recent advances in machine learning technology have opened a new era in image processing, especially in removing noises in images. The performance of this new technique is far surpassing the conventional image processing methods, which made the technique widely accepted [13,14]. However, application of the machine learning-based image processing is mostly limited to non-scientific purposes. In light of the remarkable denoising performance of neural networks and the limited data acquisition time in spectroscopic experiments, introduction of the machine learning-based denoising can bring a significant impact on acquisition and analysis of data in spectroscopic experiments. We also note recent studies in which successful application of machine learning has been demonstrated in feature extraction from spectroscopic data [15], self-energy analysis [16], x-ray structure refinement [17-19], and ultrasound spectroscopy [20].

These examples show that machine learning can also be a useful tool in condensed matter physics. Here, we demonstrate a deep learning-based denoising method for ARPES data. The proposed method utilizes a deep convolutional neural network to discriminate between noise and intrinsic signals. When the denoising is applied to noisy data for which noise and signal levels are comparable, unlike conventional denoising methods, the intrinsic information seemingly invisible in noisy spectral data is made visible. Our proposed method can drastically reduce the total acquisition time and makes it possible to overcome the limit in the data acquisition time, one of the most serious constraints in spectroscopic experiments. This, in turn, enables us to fully exploit the advantages of multidimensional measurements. Moreover, the method can be applied to any techniques that acquire multidimensional data and thus suffer from statistical noise due to shorter than desired data acquisition time.

5.2 Methods

5.2.1 Generation of training dataset

The training dataset of the neural network consists of pairs of original and generated data. The neural network is advised to generate high-count data (high SNR) from low-count data (low SNR). The low-count data can be randomly simulated from the high-count data since the count distribution is known to follow the Poisson distribution [see Fig. 5.8(a)] [15,21]. The generation of low-count data can be considered as the inverse

process of acquisition or denoising since the acquisition or denoising converts the low-count data to high-count data. Thus, only high-count data are required to construct the training dataset, which allows us to utilize readily available high-count ARPES data. Furthermore, the proposed random generation method augments the training dataset, preventing the neural network from being overfitted. Considering the fact that training of the neural network generally requires numerous data and corresponding labeling, the proposed random generation method is a cost-effective way. The generation of the training dataset is based on the assumption that the count follows the Poisson distribution[15,21]. If the total count of data is large enough, the count at a pixel divided by the total count converges to the probability of the Poisson distribution, $\lim_{N\to\infty} \frac{n_{ij}}{N} = P_{ij}$, where n_{ij} denotes counts at pixel (i, j), N denotes the total count in data, and Pij denotes the probability that an electron enters pixel (i, j) when one electron is introduced. Note that n_{ij} and P_{ij} satisfy the following equations, respectively:

$$\sum n_{ij} = N, \sum P_{ij} = 1.$$

The probability can be considered as the intrinsic information that can be obtained from the experiment. If the probability is known, one can randomly simulate experimental data with an arbitrary total count. Note that n_{ij}/N is not exactly the same as P_{ij} in ARPES data since the total count of ARPES data is a finite value. We chose the high-count training data, which have a sufficiently high total count so that the high-count data have minimum noise and n_{ij}/N is close to P_{ij}. Even though the high-count data

still have finite noise, the denoising neural network produces noise-free data, since the network is not able to learn to produce noise due to the random nature of the noise. The total count in the simulated low-count data ranges from 9 $\times 10^3$ to 3×10^6 in (300, 300) grids. Thus, the average count per pixel ranges from 0.1 to 33.3. The wide range of the total counts of the low-count training datasets ensures that the network can denoise data with any statistics. The distribution of the total count in low-count data is set to be log-weight of the total count, so a higher probability is expected for lower total count data.

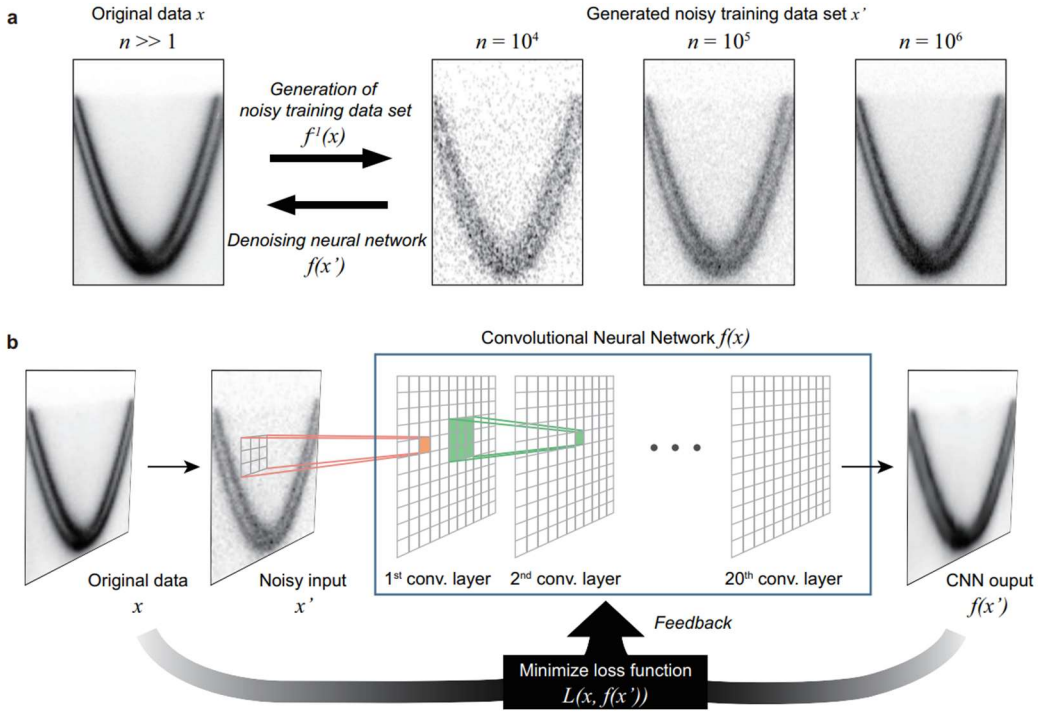

Figure 5.1. Overall training sequence of the denoising neural network. (a) Schematic for the generation of a noisy training dataset. n denotes the number of counts in the spectrum.

x denotes original data, and x´ denotes noisy data generated from original data x. The denoising process is denoted as $f(x)$, while the generation of the noisy training dataset, which is the inverse process of denoising, is denoted as $f^{-1}(x')$. The data used here are Au(111) surface state ARPES data. (b) Schematic of training the denoising neural network.

5.2.2 Training process of the denoising neural network

The overall training sequence of the neural network is described in Fig. 5.1(b). From the original high-count data x, noisy data x' are generated. Then, the convolutional neural network generates denoised data $f(x')$ from the noisy input. The size of the training data is set to be 300×300. A deep neural network of 20 convolutional layers is adopted to exploit the global contextual information. The structure of the network is based on the network proposed elsewhere [22]. Each layer of the convolutional neural network has a filter number of 64 and a filter size of 3. After each convolutional layer, the result is passed to a parametric rectifier unit to produce the non-linearity of the network [23]. By calculating the loss function $L(x, f(x'))$, the performance of the denoising neural network is determined. The loss function is defined as the weighted sum of mean absolute error (MAE) and multiscale structural similarity [24,25]. Details on the loss function are described in Appendix C. The loss is backpropagated to adjust the parameters used in the neural network [26]. An Adam optimizer is adopted to train the network for 150 epochs [27]. The learning rate is initially set to be 5×10^{-4} and multiplied

by 0.1 after every 50 epochs for a good convergence. For the training dataset, 50 different high-count ARPES data are used and, for every original data, 50 low-count data are randomly generated, resulting in a total of 2500 different low-count data. Note that the FeSe, Bi-2212, and Bi2Te3 data in Figs. 5.2–4, respectively, are not included in the training dataset. As a data augmentation, the dataset is randomly rotated or flipped, and the brightness of the data is also randomly adjusted during the training.

5.3 Results

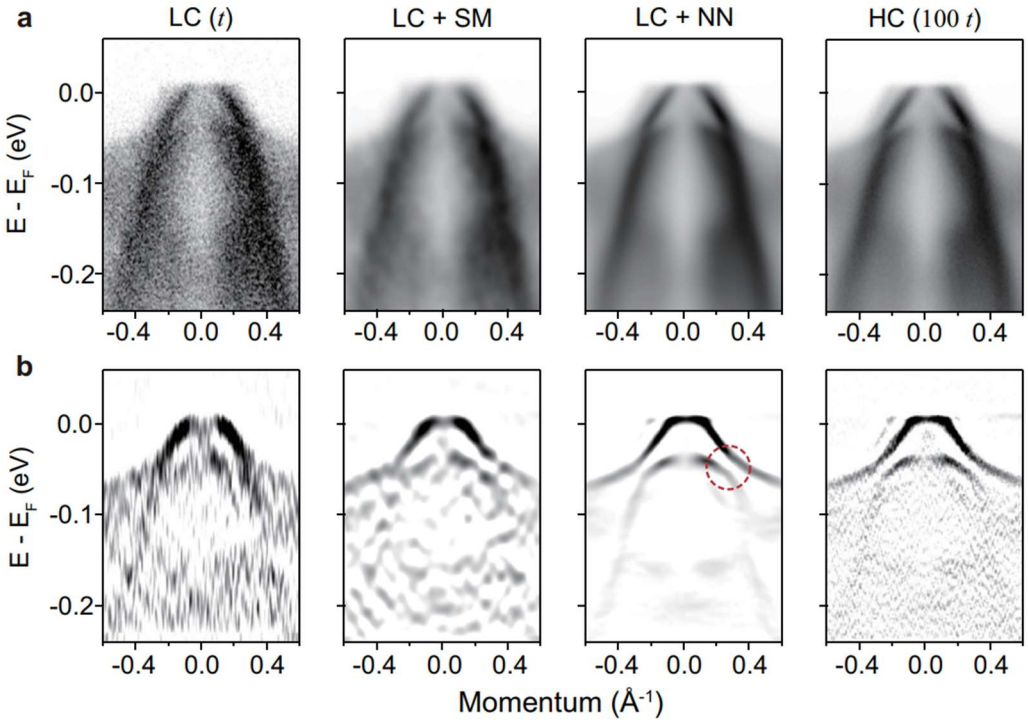

Figure. 5.2. Denoising results. (a) FeSe ARPES data along the M–Γ–M cut and denoising results. LC and HC denote low-count and high-count data, respectively. t denotes a unit acquisition time. The low- and high-count data are acquired for t and 100t, respectively.

SM and NN denote the Gaussian smoothing and denoising neural network, respectively. (b) Corresponding second-derivative results of (a). The red dotted circle represents the hybridization gap between d_{xy} and $d_{xz/yz}$ orbitals.

The result of the denoising neural network is demonstrated in Fig. 5.2(a). We took ARPES data of FeSe along the M–Γ–M cut for acquisition time t (left) and 100t (right) where t is a unit measurement time. The data acquired for t and 100t are denoted as low-count (LC) and high-count (HC) data, respectively. The LC data are used as the input to the denoising neural network, and the HC data are compared with the denoised data. The LC data show a high level of noise due to the low total count. The network produces noise-free data (middle panel), even though the input data are quite noisy. The LC data after the denoising neural network (LC + NN) are comparable to the HC data, showing almost the same features. Yet, we note that small features of the denoised data are a bit blurry due to the lack of information in the LC data. To visualize the band structure more clearly, we plot in Fig. 5.2(b) the second derivative of the data. Band dispersions from the LC data are barely visible. On the other hand, the second derivative of the denoised data in the middle panel shows very clear band dispersions, especially the hybridization gap between d_{xy} and $d_{xz/yz}$ orbitals at ±0.3 $Å^{-1}$ as indicated by a red dotted circle, which is not resolved in the original LC data [28,29]. Note that, since the noise is removed after the denoising neural network, the second derivative of the denoised data shows clean spectra, whereas the HC data have residual noise despite the long acquisition time.

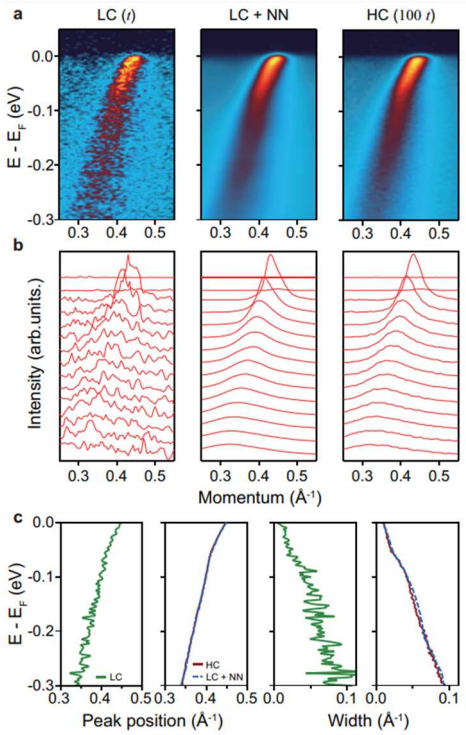

Figure. 5.3. Line shape analysis results. (a) Denoising results of ARPES data from Bi-2212 along the nodal cut. (b) Momentum distribution curves (MDCs) of the data in (a). (c) Peak positions (left) and widths (right) obtained from MDC fitting results of (b).

To verify the validity of the denoising neural network in a quantitative way, we conducted line shape analysis on denoised Bi-2212 data taken along the nodal cut. As can be seen in Fig. 5.3(a), the denoising neural network preserves intrinsic band structure while removes the noise. Removal of the noise is more clearly seen in the momentum distribution curves (MDCs) of the data depicted in Fig. 5.3(b). Line shape analysis was conducted by fitting the MDCs to obtain the peak position and width as depicted in Fig.

5.3(c). The fitting results of LC + NN and HC data are almost identical, directly demonstrating that the denoising neural network preserves the quantitative information of the band structure. We wish to point out that the well-known 70 meV kink at the nodal point is clearly resolved for both LC + NN and HC data [30,31], whereas the fitting result of the raw LC data is too noisy to identify the kink position.

5.4 Discussion

5.4.1 Understanding effectiveness of denoising neural network

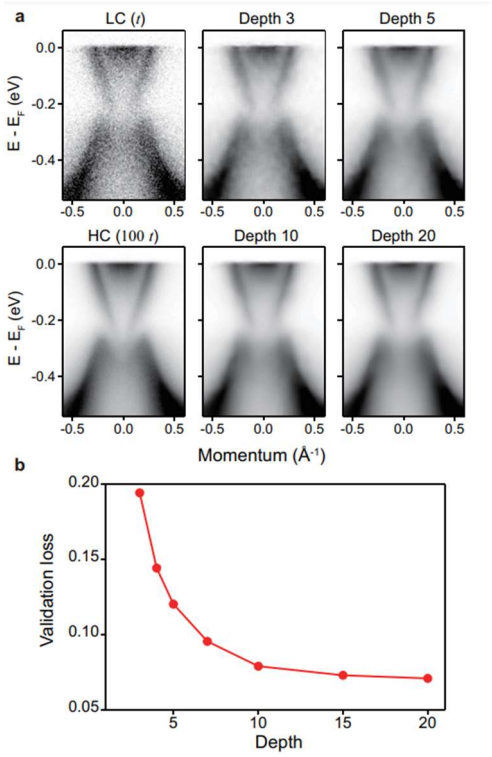

Figure. 5.4. Depth dependent denoising results. (a) ARPES data of Bi_2Te_3 along the K–

Γ−K cut and depth dependent denoising results. Depth denotes the number of convolutional layers in the denoising neural network. (b) Validation loss $L(x, f(x'))$ as a function of the depth.

The reason why the deep learning-based denoising is effective for ARPES data may be summarized into one sentence; the neighboring pixel values in ARPES data are correlated with each other. Two major factors contribute to the correlation. First, the typical dimension for ARPES features is larger than the data pixel size, leading to occupation of several pixels for any feature. Thus, if the value at a pixel is large, it is likely for neighboring pixels to have a large value. Second, the length scale over which the band structure changes is larger than the data pixel size. Hence, the band structure does not change abruptly over the length scale of the pixel. This means that the band structure has an approximate translational symmetry in a short length scale. Even if the information at a pixel is corrupted with noise, the value at the pixel can be recovered from the most statistically probable value inferred from adjacent pixel values. Therefore, a dataset carries more information than just the pixel-wise sum of information. With the additional information, the seemingly imperfect information of the noisy data can be recovered.

In order to extract such a kind of contextual information, the neural network should accept global information of data. Since the receptive field of a convolutional neural network is $(2D + 1) \times (2D + 1)$ for a depth D network with a filter size of 3, a deeper network of a larger D receives more global information [22,32]. Here, depth means the number of convolutional layers in a neural network. For a large receptive area, we

adopted a convolutional neural network of 20 layers. We experimentally show in Fig. 5.4 that a deeper network tends to work better. We took LC and HC ARPES data of a Bi_2Te_3 thin film grown on a Si(111) substrate along the K–Γ–K cut [see Fig. 5.4(a)]. The LC data are then passed to the denoising neural network with different numbers of convolutional layers. It is seen that as the depth of the denoising neural network increases, the noise is better removed and the denoised data become more similar to the HC data. In Fig. 5.4(b), the validation loss $L(x, f(x'))$ is plotted as a function of the depth to visualize the tendency more clearly. The validation dataset consists of 20 pairs of LC and HC data obtained from ARPES measurements. The validation loss monotonically decreases with increasing depth. Generally, a deeper network tends to work better if the network is not overfitted [32]. We note that the network deeper than 20 layers could not be stably trained due to gradient vanishing/exploding. Further studies are needed to train a deeper network. Considering the mechanism of the denoising neural network, it is expected that the network does not work well for data that are very different from the training data. For instance, we found that denoising performance for data with a large background was not very good since very few datasets with high levels of background were included in the training dataset. This point may be improved by including more training data with a variety of features.

5.4.2 Application to higher-dimensional data

Finally, we discuss possible application of the denoising neural network to higher-

dimensional data. Since the basic principle of denoising is the inference from adjacent pixel values, better denoising performance is expected if the data have more neighboring pixels. That is, there is much more contextual information that can be extracted from neighboring pixels in higher-dimensional data and the denoising neural network should work better. For the same reason, the denoising neural network may not work well for one dimensional spectra due to a relatively small number of neighboring pixels. Considering the fact that data acquisition in a multidimensional phase space takes a long time i.e. ARTOF analyzers, the denoising neural network will be a method to alleviate the time constraint, thereby allowing us to fully exploit the advantages of multidimensional measurements, not only for ARPES but possibly for other time demanding experimental techniques.

To check the performance of the denoising neural network depending on the dimensions of corresponding data, the neural networks are trained to denoise 2D/3D ARPES data, respectively. The 2D/3D denoising neural network adopted 2D/3D convolutional neural network, respectively. The comparison result is illustrated in Fig. 5.5. As can be seen, the denoising performance is much better for 3D denoising, which restores ground truth data from noisy data. On the other hand, the 2D denoising generates somewhat different data from ground truth. This is due to the high noise level of input data. The noise level of input data is set to be high, to compare the performance of the 2D/3D denoising neural networks.

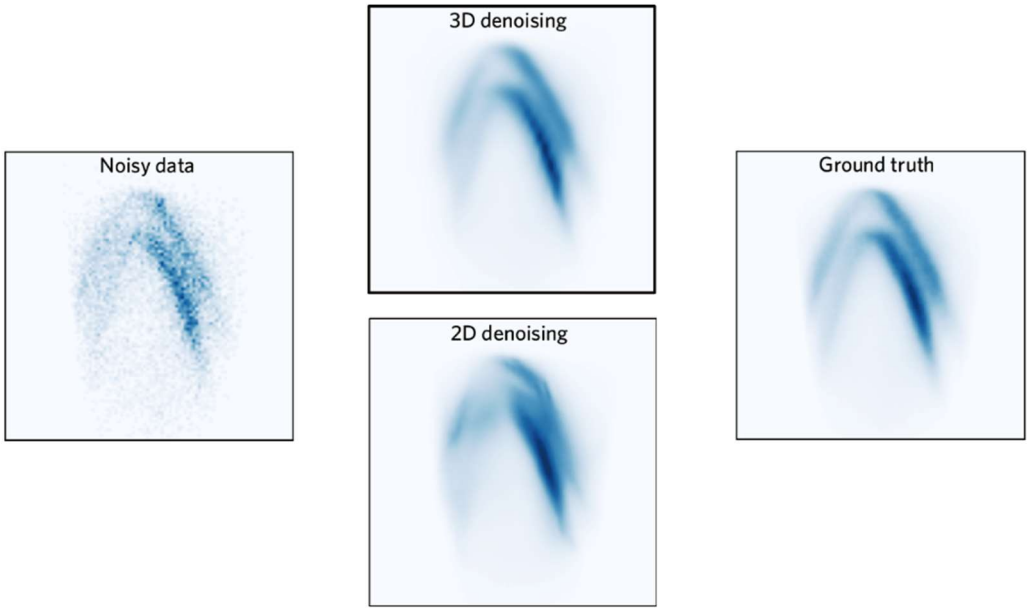

Figure 5.5 Comparison of the performance of 2D/3D denoising.

5.5 Summary and outlook

We have demonstrated that the network not only reduces the acquisition time but also reduces the noise of data to an experimentally unreachable level. If trained properly, this scheme can also be used for distributions other than Poisson. The thorough removal of the noise opens up a new route for data analysis techniques for which noise is an apparent obstacle, such as deconvolution [33] and self-energy analysis [34]. That is, the denoising neural network can be used as the base layer for other data analysis techniques, which calls for further studies on artificial intelligence-based data analysis methods. It is also noteworthy that open-source Python-based data analysis packages for ARPES and other

multidimensional experimental techniques were recently demonstrated [35,36]. Considering the open source nature of these packages along with the high expandability of Python, implementation of our deep learning-based denoising method into one of the Python-based data analysis packages can be easily achieved. In addition, since the time required to denoise an ARPES dataset typically takes less than a few seconds, the implementation will allow us to denoise data in real time while analyzing and visualizing data. This would provide a new deep learning-based data analysis platform for the ARPES community.

5.6 Appendix

5.6.1 Training dataset

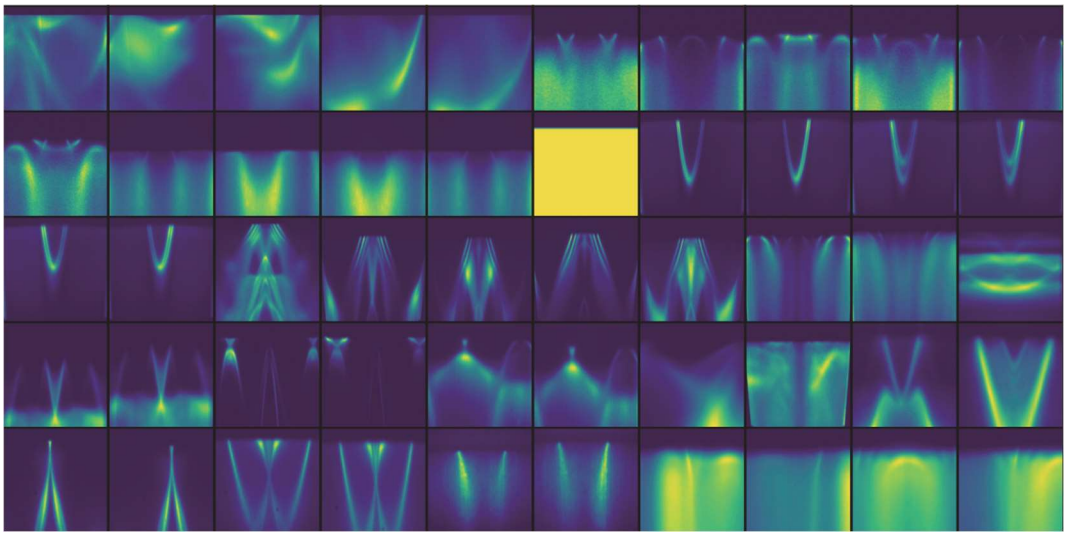

Figure. 5.6. Plot of the dataset used in the training.

The data used for training are plotted in Fig. 5.6. Data complying with the following conditions were used as training data. First, the data must have a sufficiently high total count to have a low level of noise. Second, the data have no artifacts from detector inhomogeneity.

5.6.2 Low-count data for hemispherical analyzers

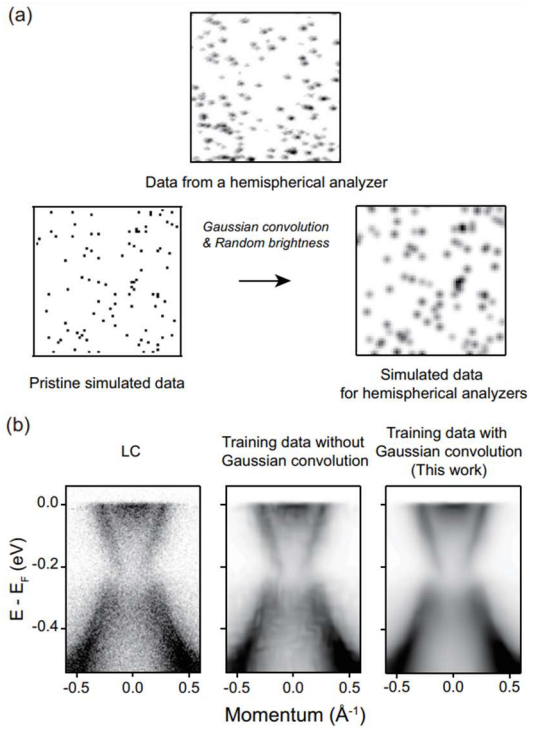

Figure. 5.7. (a) Examples of the data from a hemispherical analyzer and simulated data. (b) ARPES data of Bi2Te3 and training data dependent denoising results.

The low-count data generated from the aforementioned method has pixel-wise

discrete values. However, the data acquired from a hemispherical analyzer consist of counts occupying several pixels, as described in Fig. 5.7(a), since the detector of a hemispherical analyzer measures an impinged signal on a phosphor screen using a CCD camera. To simulate the experimental results obtained with a hemispherical analyzer, the simulated data are convoluted with a Gaussian function with random peak intensities and widths. Without such Gaussian convolution, denoising the data from a hemispherical analyzer shows bad performance [see Fig. 5.7(b)].

5.6.3 Loss function

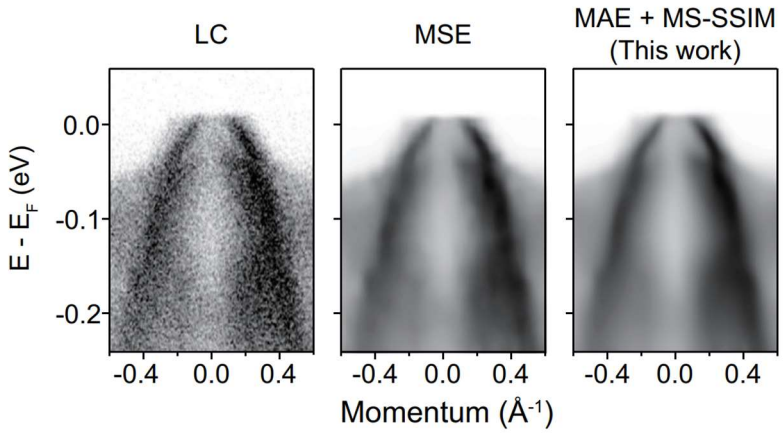

Figure 5.8. (a) Examples of the data from a hemispherical analyzer and simulated data. (b) ARPES data of Bi2Te3 and training data dependent denoising results.

The loss function adopted in this work is a weighted sum of mean absolute error (MAE) and multiscale structural similarity (MS-SSIM). The conventional mean squared error (MSE) has a weak penalty for a small difference. Hence, the denoised result is

blurry since making the data blurry is an easy way to minimize MSE loss. We therefore adopted a new loss function consisting of MAE and MS-SSIM as described elsewhere, $L = (1-\alpha)\cdot L_{MAE} + \alpha \cdot L_{MS-SSIM}$, where α is set to be 0.7. The MAE loss has a higher penalty for a small difference compared to MSE loss, so the result is expected to be less blurry. The MS-SSIM loss catches a similarity over a wide range of the data compared to MSE loss or MAE loss, which calculates the pixel-wise difference. Thus, the result is perceptually more plausible and the MS-SSIM loss ensures overall similarity. The comparison results of MSE loss and the loss used in this work are plotted in Fig. 5.8.

5.6.4 Overfitting

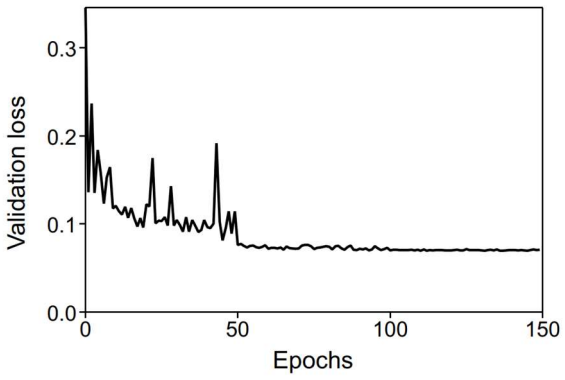

Figure 5.9. Plot of validation loss during the training.

Overfitting is one of the most serious issues in deep learning. Generally, the overfitting occurs when the training dataset is small compared to the size of the neural network. We checked the overfitting by monitoring validation loss during the training

since the increase in the validation loss is a representative symptom of the overfitting. As shown in Fig. 5.9, the validation loss converges to a value at the end of the training. From the result, we judged that the model is not overfitted.

References

[1] Y. Kim *et al.*, Review of Scientific Instruments **92**, 073901 (2021).

[2] A. Damascelli, Z. Hussain, and Z.-X. Shen, Reviews of modern physics **75**, 473 (2003).

[3] A. Damascelli, Physica Scripta **2004**, 61 (2004).

[4] X. Zhou, S. He, G. Liu, L. Zhao, L. Yu, and W. Zhang, Reports on Progress in Physics **81**, 062101 (2018).

[5] J. A. Sobota, Y. He, and Z.-X. Shen, Reviews of Modern Physics **93**, 025006 (2021).

[6] K. Medjanik *et al.*, Nature Materials **16**, 615 (2017).

[7] M. Keunecke *et al.*, Review of Scientific Instruments **91**, 063905 (2020).

[8] T. Reber, N. Plumb, J. Waugh, and D. Dessau, Review of Scientific Instruments **85**, 043907 (2014).

[9] Y. Ishida, T. Otsu, A. Ozawa, K. Yaji, S. Tani, S. Shin, and Y. Kobayashi, Review of Scientific Instruments **87**, 123902 (2016).

[10] S. Hellmann, T. Ott, L. Kipp, and K. Rossnagel, Physical Review B **85**, 075109 (2012).

[11] S. Hofmann, *Auger-and X-ray photoelectron spectroscopy in materials science: a user-oriented guide* (Springer Science & Business Media, 2012), Vol. 49.

[12] P. Zhang, P. Richard, T. Qian, Y.-M. Xu, X. Dai, and H. Ding, Review of Scientific Instruments **82**, 043712 (2011).

[13] K. Zhang, W. Zuo, Y. Chen, D. Meng, and L. Zhang, IEEE transactions on image processing **26**, 3142 (2017).

[14] E. Chen, Advances in neural information processing systems, 341 (2012).

[15] H. Peng *et al.*, Review of Scientific Instruments **91**, 033905 (2020).

[16] Y. Yamaji, T. Yoshida, A. Fujimori, and M. Imada, Physical Review Research **3**, 043099 (2021).

[17] P. M. Vecsei, K. Choo, J. Chang, and T. Neupert, Physical Review B **99**, 245120 (2019).

[18] W. B. Park, J. Chung, J. Jung, K. Sohn, S. P. Singh, M. Pyo, N. Shin, and K.-S. Sohn, IUCrJ **4**, 486 (2017).

[19] H. Liang, V. Stanev, A. G. Kusne, and I. Takeuchi, Physical Review Materials **4**, 123802 (2020).

[20] S. Ghosh, M. Matty, R. Baumbach, E. D. Bauer, K. A. Modic, A. Shekhter, J. Mydosh, E.-A. Kim, and B. Ramshaw, Science advances **6**, eaaz4074 (2020).

[21] Y. He, Y. Wang, and Z.-X. Shen, Review of Scientific Instruments **88**, 073903 (2017).

[22] J. Kim, J. K. Lee, and K. M. Lee, in *Proceedings of the IEEE conference on computer vision and pattern recognition*2016), pp. 1646.

[23] K. He, X. Zhang, S. Ren, and J. Sun, in *Proceedings of the IEEE international conference on computer vision*2015), pp. 1026.

[24] Z. Wang, E. P. Simoncelli, and A. C. Bovik, in *The Thrity-Seventh Asilomar Conference on Signals, Systems & Computers, 2003* (Ieee, 2003), pp. 1398.

[25] H. Zhao, O. Gallo, I. Frosio, and J. Kautz, IEEE Transactions on computational imaging **3**, 47 (2016).

[26] Y. LeCun, B. Boser, J. S. Denker, D. Henderson, R. E. Howard, W. Hubbard, and L. D. Jackel, Neural computation **1**, 541 (1989).

[27] D. P. Kingma and J. Ba, arXiv preprint arXiv:1412.6980 (2014).

[28] S. Huh *et al.*, Communications Physics **3**, 1 (2020).

[29] P. Zhang *et al.*, Physical Review B **91**, 214503 (2015).

[30] D. Garcia and A. Lanzara, Advances in Condensed Matter Physics **2010** (2010).

[31] T. Kondo, Y. Nakashima, W. Malaeb, Y. Ishida, Y. Hamaya, T. Takeuchi, and S. Shin, Physical review letters **110**, 217006 (2013).

[32] K. He, X. Zhang, S. Ren, and J. Sun, in *Proceedings of the IEEE conference on computer vision and pattern recognition*2016), pp. 770.

[33] J. Rameau, H.-B. Yang, and P. Johnson, Journal of Electron Spectroscopy and Related Phenomena **181**, 35 (2010).

[34] A. Kordyuk, S. Borisenko, A. Koitzsch, J. Fink, M. Knupfer, and H. Berger, Physical Review B **71**, 214513 (2005).

[35] K. Kramer and J. Chang, Journal of Open Source Software **6**, 2969 (2021).

[36] C. Stansbury and A. Lanzara, SoftwareX **11**, 100472 (2020).

Chapter 6

Summary & Remarks

This thesis starts with introducing the background of iron-based superconductors. The main focus is physical properties of iron-based superconductors from a perspective of electronic structures. In particular, bond angle dependent physics is described in detail, which is a prime parameter determining the physical properties of iron chalcogenide superconductors.

In chapter 2, setup of the laser-based ARPES system is introduced. The purpose of the setup is to reveal low-energy electronic structures of iron chalcogenide. The components of the laser-based ARPES system, especially ARTOF analyzer, fiber-based laser are discussed in detail.

In chapter 3, results on the strongly correlated iron chalcogenide, FeTe is discussed. By utilizing the laser-based ARPES and various tools that can measure transport properties or local density of states, it is revealed that the Kondo hybridization plays an important role determining the physical and magnetic properties of FeTe.

In chapter 4, results on the superconducting iron chalcogenide, Fe(Te,Se) is discussed. The superconducting gap structures were directly measured, which shows strongly anisotropic gap structure. This result implies that the superconducting gap symmetry deviates from conventional s+- wave superconductivity. The change of superconducting gap symmetry is driven by strong correlation effect.

In chapter 5, deep learning-based denoising method is introduced. By utilizing the technique, the long acquisition time of ARTOF analyzer can be drastically reduced. This is enabled by the fact that the denoising performance is much better for multidimensional data since there are more adjacent pixels (voxels for three-dimensional data).

The development of laser-based ARPES system with novel combination of ARTOF analyzer, fiber-based laser, and deep learning can be a new ARPES platform, which makes the data acquisition much faster without space-charge effect.

Chapter 7

Publication List

1. **Electric control of two-dimensional Van Hove singularity in oxide ultra-thin films**

   D. Kim*, Y. S. Kim*, B. Sohn †, M. Kim, B. Kim, T. W. Noh, C. Kim†

   Advanced Materials, accepted.

2. "**Signature of Kondo hybridisation with an orbital-selective Mott phase in 4d $Ca_{2-x}Sr_xRuO_4$**

   M. Kim, J. Kwon, C. H. Kim, **Y. S. Kim**, D. Chung, H. Ryu, J. Jung, B. S. Kim, D. Song, J. D. Denlinger, M. Han, Y. Yoshida, T. Mizokawa, W. Kyung †, C. Kim†

   npj Quantum Mater. **7**, 59 (2022).

3. **Strain-controlled evolution of electronic structure indicating topological phase transition in the quasi-one-dimensional superconductor $TaSe_3$**

   J. Hyun*, M. Y. Jeong*, M.-C. Jung, Y. Lee, **Y. S. Kim**, S. Jung, B. Seok, J. Song, C. Lim, J. Cha, G. Lee, Y. An, M. Hashimoto, D. Lu, J. D. Denlinger, S. W. Kim, C.

Kim, M. J. Han, S. Kim †, Y. Kim†

Phys. Rev. B. **105**, 11 (2022).

4. Kondo interaction in FeTe and its potential role in the magnetic order

Y. S. Kim, M. Kim, M.-S. Kim, C.-M. Cheng, J. Choi, S. Jung, D. Lu, J. H. Kim, S. Cho, D. Song, D. Oh, L. Yu, Y. J. Choi, H.-D. Kim, J. H. Han, Y. Jo, J. Seo, S. Huh †, C. Kim †

arXiv:2203.06432 (Review in progress: Nature Communications)

5. Heteroepitaxial control of Fermi liquid, Hund metal, and Mott insulator phases in the single-atomic-layer limit

J. R. Kim*, B. Sohn*, H. J. Lee*, S. Lee, E. K. Ko, S. Hahn, S. Lee, **Y. S. Kim**, D. Kim, H. J. Kim, Y. Kim, J. Son, C. H. Ahn, F. J. Walker, A. Go, M. Kim, C. H. Kim †, C. Kim †, T. W. Noh †

Advanced Materials, accepted.

6. Cu doping effects on the electronic structure of $Fe_{1-x}Cu_xSe$

S. Huh*, Z. Lu*, **Y. S. Kim**, D. Kim, S. Liu, M. Ma, L. Yu †, F. Zhou, X. Dong, C. Kim †, Z. Zhao

Phys. Rev. B **105**, 245140 (2022).

7. B_{1g}-Phonon Anomaly Driven by Fermi Surface Instability at Intermediate Temperature in $YBa_2Cu_3O_{7-\delta}$

D. Oh, D. Song, **Y. S. Kim**, S. Miyasaka, S. Tajima, J. M. Bok, Y. Bang, S. R. Park, C. Kim †

Phys. Rev. Lett. **127**. 277001 (2021).

8. Observation of spin-dependent dual ferromagnetism in perovskite ruthenates

S. Hahn*, B. Sohn*, M. Kim, J. R. Kim, S. Huh, **Y. S. Kim**, W. Kyung, M. Kim, D. Kim, Y. Kim, T. W. Noh, J. H. Shim, C. Kim †

Phys. Rev. Lett. **127**, 256401 (2021).

9. Sign-tunable anomalous Hall effect induced by two-dimensional symmetry-protected nodal structures in ferromagnetic perovskite thin films

B. Sohn*, E. Lee*, S. Y. Park, W. Kyung, J. Hwang, J. D. Denlinger, M. Kim, D. Kim, B. Kim, H. Ryu, S. Huh, J. S. Oh, J. K. Jung, D. Oh, **Y. S. Kim**, M. Han, T. W. Noh, B.-J. Yang †, C. Kim †

Nat. Mater. **20**, 1643-1649 (2021).

10. Observation of metallic electronic structure in a single-atomic-layer oxide

B. Sohn*, J. R. Kim*, C. H. Kim, S. Lee, S. Hahn, **Y. S. Kim**, S. Huh, D. Kim, Y. Kim, W. Kyung, M. Kim, M. Kim, T. W. Noh †, C. Kim †

Nat. Commun. **12**, 6171 (2021).

11. Deep learning-based statistical noise reduction for multidimensional spectral data

Y. S. Kim, D. Oh, S. Huh, D. Song, S. Jeong, J. Kwon, M. Kim, D. Kim, H. Ryu, J. Jung, W. Kyung, B. Sohn, S. Lee, J. Hyun, Y. Lee, Y. Kim, C. Kim †

Rev. Sci. Instrum. **92**, 073901 (2021).

12. A compact and stable incidence-plane-rotating second harmonics detector

S. H. Kim, S. Jung, B. Seok, **Y. S. Kim**, H. Park, T. Otsu, Y. Kobayashi, C. Kim, Y. Ishida †

Rev. Sci. Instrum. **92**, 043905 (2021).

13. Momentum dependent $d_{xz/yz}$ band splitting in LaFeAsO

S. Huh, **Y. S. Kim**, W. Kyung, J. Jung, R. Kappenberger, S. Aswartham, B. Büchner,

J. M. Ok, J. S. Kim, C. Dong, J. P. Hu, S. H. Cho, D. W. Shen, J. D. Denlinger, Y. K. Kim, C. Kim †

Sci. Rep. **10**, 19377 (2020).

14. Work function seen with sub-meV precision through laser photoemission

Y. Ishida †, J. K. Jung, M. S. Kim, J. Kwon, **Y. S. Kim**, D. Chung, I. Song, C. Kim, T. Otsu, Y. Kobayashi

Commun. Phys. **3**, 158 (2020).

15. Classification of the symmetry of photoelectron dichroism broken by light

Y. Ishida †, D. Chung, J. Kwon, **Y. S. Kim**, S. Soltani, Y. Kobayashi, A. J. Merriam, L. Yu, C. Kim

arXiv:2007.02178

16. Rotation of reflectivity anisotropy due to uniaxial strain along $[110]_{tetr}$ in the electron-doped Fe-based superconductor $Ba(Fe_{0.955}Co_{0.045})_2As_2$

I. Kwak, S. Huh, M.-C. Lee, **Y. S. Kim**, B. Lee, Y. S. Lee, C. W. Seo, B. C. Park, T.

Wolf, C. Kim, T. W. Noh †, K. W. Kim †

Phys. Rev. B **101**, 165136 (2020).

17. Magnetic field detwinning in FeTe

Y. S. Kim, S. Huh, J. Kim, Y. Choi, C. Kim †

Prog. Supercond. Cryog. **21**, 6-8 (2019).

국문 초록

철-칼코겐 화합물 초전도체에서의 레이저 기반 분광학 연구

김윤식

물리천문학부

서울대학교 대학원

철기반 초전도체는 다양한 발현 현상과 일반적이지 않은 초전도 현상을 보인다. 이 덕분에 강상관계 물질에 대한 연구는 철기반 초전도체의 발견과 함께 새로운 국면을 맞이하였다. 철기반 초전도체에서 다중 궤도가 줄 수 있는 자유도는 자성 상태, 네마틱 상, 그리고 궤도 선택적 물리 등과 같은 새로운 현상을 가능하게 한다. 하지만 철기반 초전도체에 대한 많은 관심에도 불구하고 철기반 초전도체의 낮은 에너지 전자 구조는 아직까지도 잘 밝혀지지 않았는데, 이는 낮은 초전도 임계 온도와 강한 전자 간 상호작용으로 인한 큰 재규격화에 기인한다. 따라서 철기반

초전도체의 낮은 에너지 전자 구조를 파악하기 위해서는 레이저 기반 분광학 기법과 같은 고분해능을 가진 실험 장치를 사용하여야 한다. 특히, 레이저 기반 각분해 광전자 분광법을 이용한다면 이들 시스템의 낮은 에너지 전자 구조가 직접적으로 파악할 수 있다. 이 졸업 논문에서는 고분해능을 가진 각분해 광전자 분광 장비 개발과 그 장비로 측정한 철기반 초전도체에서의 결과가 소개되어 있다. 여기서 레이저는 광섬유로 만들어져 있어 전체적인 크기가 작고 안정적으로 구동될 수 있다. 만들어진 각분해 광전자 분광 시스템은 비행시간 전자 분석기를 이용한다. 비행 시간 전자 분석기의 고질적인 단점인 긴 측정 시간은 심층 학습을 기반으로 한 노이즈 감쇄 기법을 이용하여 보완되었다. 철기반 초전도체에 대한 결과는 첫째, FeTe 에서 콘도 격자 현상, 둘째, Fe(Te,Se) 에서 강한 비등방 초전도 틈과 관련한 내용이다. 개발된 장비를 이용한 철기반 초전도체에서 저에너지 전자 구조의 성공적인 측정은 일반적이지 않은 초전도 현상에 대한 연구를 불러일으킬 뿐만 아니라 새로운 각분해 광전자 분광 시스템의 입증이라는 데 그 중요성이 있다.

주요어 : 철기반 초전도체, 철 칼코겐 화합물, 광섬유 기반 레이저, 각분해 광전자 분광학, 심층 학습, 궤도 선택적 모트 상전이, 콘도 물리

학번 : 2017-25965